Calibration of reverberation chamber for wireless measurements: Study of accuracy and characterization of the number of independent samples

Master of Science Thesis

ELENA MARIA PUCCI

Department of Signals and Systems
Division of xxx
CHALMERS UNIVERSITY OF TECHNOLOGY
Göteborg, Sweden, 2008
Report No. EX087/2008

Laurea Specialistica in Ingegneria delle Telecomunicazioni

Chalmers University of Technology

Universitá degli Studi di Siena

Calibration of Reverberation Chamber for Wireless Measurements: Study of Accuracy and Characterization of the Number of Independent Samples

Elena Maria Pucci

Relatore
Prof. Stefano Maci

Correlatori
Prof. Per-Simon Kildal
Dr. Ulf Carlberg

Anno Accademico 2007-2008

Calibration of Reverberation Chamber for wireless measurements: study of accuracy and characterization of the number of independent samples
Elena Maria Pucci

This thesis has been prepared using LaTeX.

Abstract

Traditionally, the Reverberation Chamber (RC) has been used for EMC testing, but recently it has been developed for measuring antennas and mobile terminals designed for wireless applications. It is a metal cavity, large in terms of wavelength which supports several cavity modes at the operation frequency. The modes are stirred by appropriate stirring methods producing a rich scattering environment with Rayleigh distribution of the received complex signal amplitude. Due to the statistical nature of the electromagnetic field inside the chamber, the RC is ideal for simulating in compact space the behavior of mobile terminals operating in fading environments as the urban and the indoor ones. The rapidly growing use of the RC for these kinds of applications has developed the necessity of fast and accurate measurements. In addition, the accuracy is typically more critical in antenna efficiency measurements than in EMC tests. Therefore, studies of the mechanisms that may affect the measurements accuracy are becoming of great interest. If the stirrers are able to perform a proper stirring of the excited modes, a large number of independent field samples are created. The independency of those samples is of great importance in quantifying the uncertainty of a test performed in the cavity. This thesis determines the importance of different steps in the procedure of calibrating a RC in order to improve the accuracy for wireless measurements. The study is performed using the Bluetest High Performance RC at Chalmers University of Technology. By measuring with several stirring configurations, number of stirrer positions and chamber loading, we are able to show how the number of independent samples varies when different stirring techniques are used and extra lossy objects are present inside the chamber. In addition, a new theoretical formula for the estimation of the number of independent samples when different stirring methods are applied is proposed. The results show that the number of independent samples estimated with the new formula and the one measured have a poor agreement at the lower frequencies compared to high fre-

quencies. This work will show that the reason of this mismatch is a residual error due to direct coupling between the transmitting and the receiving antennas which will be negligible only at high frequencies. By removing such term, better agreement between theory and measurements is found at the lower frequencies. This work also shows that among all stirring methods, the platform stirring provides the best accuracy. Moreover, this thesis presents that when platform stirring is not used, the accuracy can be increased by applying complex S_{21} stirring, which consists in removing the mean over all the stirrer positions from the received complex signal S_{21}. This mean represents the direct coupling.

Preface

This thesis is in fulfillment of the Master degree in Telecommunication Engineering at University of Siena (Italy). The work was carried out at the Antenna Group, Department of Signals and Systems, at Chalmers University of Technology (Sweden) between January and July 2008. The internship activity in Antenna Group has been supported by University of Siena within the ERASMUS exchange program.
The thesis work has been supervised by Professor Per-Simon Kildal and Doctor Ulf Carlberg from Chalmers University of Technology.

Acknowledgements

First, I would like to thank Prof. Per-Simon Kildal for giving me the opportunity of working on this project. Thanks for your guidance and for supervising me with the best support since the first day I joined the Antenna Group. My sincere gratitude goes to my second supervisor, Dr. Ulf Carlberg, for helping me during the whole work. I really appreciated not only your help with Matlab but also the moments of fun we shared. I also want to thank Antonio Sorrentino, who worked with me on this project. Your feedback and knowledge in to the topic were enlightening for the success of this work.

Very special thanks go to all the members of the Antenna Group: Chen Xiaoming, Yogesh Karandikar, Daniel Nyberg, Nima Jamaly, Jian Yang, Charlie Orlenius, Jan Carlsson, Eva Rajo Iglesias and all the Master students. All you have contributed to make a very pleasant environment. Thanks not only for the help I received but also for the funny dinners, parties and nice moments we shared. I was very fortunate to have been given the change to be part of such group.

My sincerest thanks go out to my friend Guillermo for his deep friendship, and for supporting and helping me every day of these months. I truly enjoyed our coffee breaks, dinners, daily lunches and outings with the bike. Thanks for your belief in me and for inducing me on never give up.
I also want to thank all my friends from the Department of Signals and Systems. My days in Gothenburg would have been far less enjoyable without your company.

Unfortunately, I could spend only six months in Sweden, but I will keep for ever with me all my memories about this special period.

Elena

Contents

Chapter 1

Introduction

1.1 The Reverberation Chamber for Wireless Measurements

For several years the reverberation chamber (RC) has been used for measuring shielding effectiveness and EMC testing, since it is an overmoded shielded room able to improve the repeatability in emission and shielded effectiveness testing. In the last years, the RC was developed for measuring the antennas performance for wireless applications. Nowadays, many wireless systems are available and in order to study those systems, an accurate and realistic channel model is needed. Thus, every channel model needs to be validated by measurements. However, measurements are not an easy task, since a considerable amount of time is usually required and they should be performed in several environments to model all the scenarios. Moreover, the measurements systems are extremely costly. To address all this problems, the use of the RC has been proposed, since it has the advantage to be controllable and able to reproduce several times the same environments. The RC is a large metal cavity that support many resonant modes. The modes are continuously stirred so that a rich scattering environment is created inside. Therefore, the RC represents an isotropic multipath environment with a uniform field. For this reason, the reverberation chamber has been extended to characterize antennas and terminals designed for multipath environments and subject to strong fading, as diversity and MIMO systems [1], [2].

1.2 Multipath Environment

Mobile terminals are subject to a strong fading due to multipath propagation when used in urban and indoor environments. In those environments, the transmission path between the receiving and the transmitting antennas will be reflected and diffracted many times from the edges of large smooth objects, like buildings and trees, creating several wave paths that will add at the receiving side, as shown in Figure 1.1. Thus, the complex signal at the receiver side can be written as

$$S = \sum_i S_i, \tag{1.1}$$

where

$$S = S_{\mathrm{Re}} + jS_{\mathrm{Im}}. \tag{1.2}$$

Thereby, the multipath environment can be characterized by several independent incoming plane waves. This independence means that their amplitudes, phases, polarizations and angles of arrival are arbitrary relative to each other. If the line-of-sight between the two sides is absent and the number of incoming waves is large enough, the in-phase and quadrature components of the received complex signal become Gaussian, their associated magnitude

$$A = \sqrt{S_{\mathrm{Re}}^2 + S_{\mathrm{Im}}^2} \tag{1.3}$$

get a Rayleigh distribution and the phases a uniform distribution over the unit sphere, as the central limit theorem stated [3]. These are the characteristics of a Rayleigh channel model. When a predominant path exists between the transmitter and the receiver, the multipath environment is defined by the Rice fading which is characterized by the Rician K-factor. The K-factor is defined as

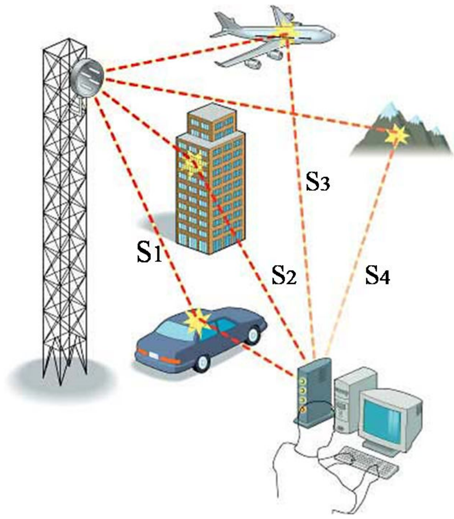

Figure 1.1: Example of a typical urban environment.

the ratio between the direct path component and the scattered components [4].

1.3 Isotropic Reference Environment

It is natural to assume that a mobile terminal can be oriented arbitrarily considering the directions in the horizontal plane. However, the terminals can have a preferred orientation relative to the vertical axis and in common environments, waves have a larger probability of coming in from close to horizontal than to vertical directions. Thus, the distribution of the angles of arrival and the polarizations are different from one environment to another. It implies that the performance of terminals and antennas depend on where they are used, which means the results of measurements cannot be transferred from one environment to another. Therefore, it is desirable to have an isotropic reference environment with polarization balance and uniform distribution of the angles of arrival in both azimuth and elevation, i.e. an environment in which all polarizations and angles of arrival are equally probable over the whole unit sphere. This simplifies the characterization of antennas and terminals in the sense that the performance becomes independent of the orientation of the antenna in the environment. In a real one, the antenna and the phone are usually used on the left and the right sides of the head with different orientations. Thus, the assumption of a reference isotropic environment is representative, since any environment will appear isotropic if the terminal is used with arbitrary orientation. The reverberation chamber can emulate an isotropic environment, giving repeatable results.

1.4 Reverberation and Anechoic Chambers

Figure 1.2 shows a simple example of applications in which the anechoic and the reverberation chambers can be used. Traditionally, antennas were designed for use in environments where there is line-of-sight (LOS) between the transmitting and the receiving antennas. Therefore, antennas were characterized in the equivalent of a free space environment, by measuring in anechoic chambers, in which the absorbent materials block reflections of the transmitted signal in order to create the free space conditions. With the development of wireless applications, the antennas has been designed for use in multipath environments as the urban and the indoor ones. In order to characterize such antennas the RC is needed, since by its metallic walls it recreates a rich scattering environment as the real one. The reverberation chamber has the advantages of being smaller and cheaper than

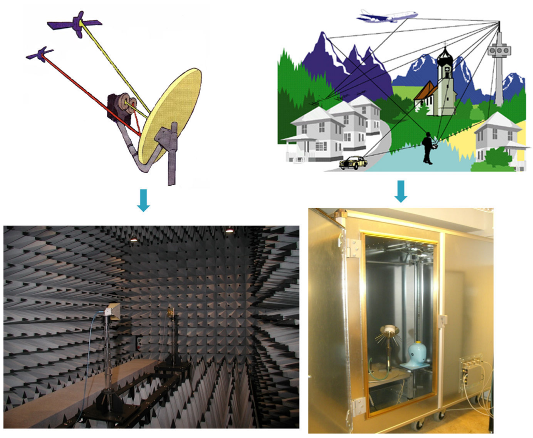

Figure 1.2: Example of typical applications in which the anechoic and the reverberation chambers are used. The anechoic chamber is used for measuring the line-of-sight between two antennas. The RC is needed for measuring antennas designed for multipath environments.

the anechoic chamber. Moreover, the measurement time is reduced. In both it is possible to measure parameters as radiation efficiency, total radiated power and receiver sensitivity, but only by the reverberation chamber it is possible to characterize the MIMO capacity and the diversity gain. A comparison between the anechoic and the reverberation chambers is shown in Figure 1.3. The only parameter we cannot measure with RC is the radiation pattern. However, we do not need of the pattern when we are interested to characterize the antenna performance in multipath environments.

Quantity	Anechoic chamber	Reverberation chamber
Size	☹	☺
Price	☹	☺
Measurement time	☹	☺
Radiation pattern	☺	☹
Radiation efficiency	☺	☺
Total radiated power TRP	☺	☺
Receiver sensitivity TIS	☺	☺
Average fading sensitivity AFS	☹	☺
Diversity gain (active terminals)	☹	☺
MIMO capacity, opportunistic scheduling and more (active terminals)	☹	☺

Figure 1.3: Comparison between anechoic and reverberation chambers.

1.5 Motivation and Objectives of this Thesis

The measurements made in reverberation chambers give back sequences of power levels needed to compute parameters as the radiation efficiency of the antenna under test. However, the field inside the chamber is statistic by nature, so that only an estimate of the mean power level is accessible from measurements. Those statistical properties ensure that such estimation is accurate only if a large number of independent power samples are created inside the chamber. The amount of independent samples depends on how well the excited modes are stirred inside the RC. Thus, the effect of the different stirring methods on the generation of a large number of independent samples is of great interest. Different stirring techniques are proposed in [5] and [6], by which an improvement of the accuracy is determined. Some models have also been proposed in [7], [8] and [9] in order to optimize the stirrers design and effectiveness. However, a critical issue is to estimate the number of independent samples obtained when different stirring methods are applied. Although some methods to determine the number of independent samples are presented in [10] and [11], a physical formula for its estimation has not been pointed out yet. Therefore, evaluating the number of independent samples still remains a great challenge. In this thesis a new physical formula for the estimation of the number of independent samples when different stirring methods are used is proposed. Measurements and experimental validation are shown. The study is performed using the reverberation chamber at Chalmers University of Technology, provided of mechanical, polarization and frequency stirrers. The purpose is also to determine the importance of the different stirring techniques in the calibration procedure of the RC. Their effects on the generation of independent samples are presented and some solutions to improve the accuracy are also proposed.

1.6 Description of the Following Chapters

- Chapter 2: A theoretical analysis of the reverberation chamber starting from the modal distribution to the chamber geometry is presented. The study includes a description of the stirring methods and their effects on the excited modes. The statistical properties of the field inside the chamber are also shown in this chapter.

- Chapter 3: Measurements setup in the RC is shown. In this chapter the measurements protocol is presented step by step. Particular attention will be paid to the calibration procedure, the chamber control software and the data processing. Preliminary results obtained from measurements are shown.

- Chapter 4: The accuracy and the number of independent samples are analyzed. A new physical formula for the estimation of the number of independent samples is presented. The formula provides the number of independent samples we can attain when different stirring techniques are used.

- Chapter 5: Measurements and results are shown. A comparison between the number of independent samples theoretical and measured is presented. The measurements are performed for several stirring methods and the effects of the different stirring techniques on the chamber accuracy will be point out. Several solutions are also presented in order to improve the accuracy and experimental validation is provided. Finally, the best case attained is determined.

- Chapter 6: Conclusions and Future work are presented.

Chapter 2

Theoretical Analysis of the Reverberation Chamber

2.1 The Reverberation Chamber as an Isotropic Multipath Environment

In the last years, the reverberation chamber has been developed for measuring the characteristics of small antennas and mobile terminals for wireless applications. It is a metal cavity which is large in terms of a wavelength so that it can support several cavity modes at the operation frequency. When a sufficient number of resonant modes exists in the chamber, a rich scattering environment is created. Due to this phenomenon, the phase information is totally lost and the E-field vector at any location in the chamber is seen as the sum of multipath plane waves with random phases [12]. This means that a statistically uniform E-field is created inside the chamber with a uniform distribution of wave directions in both azimuth and elevation. Since the number of modes is proportional to the dimensions of the chamber [13], it is necessary to increase the chamber size in order to excite as many modes as possible. However, we can virtually increase the volume of the chamber by using stirring methods since building a larger chamber can be expensive and bulky. The basic idea is to shift the eigenfrequency of the resonant modes by changing the boundary conditions of the chamber walls (i.e., change the chamber geometry). The resonant modes are stirred and perturbed by using stirring techniques, creating a large overmoded cavity with a statistically uniform field when a sufficient number of independent transmitted signals exists. This arrangement is ideally used for simulating in a compact space the behavior of mobile terminals operating in fading environments as the urban and indoor ones.

2.2 Modal Analysis

To explain how the field configurations (modes) can exist inside a reverberation chamber, we can begin by describing the case of an infinite rectangular waveguide [14]. Then, we will discuss the case of the closed rectangular cavity, which is the best ideal approximation for real reverberation chambers.

2.2.1 Rectangular Waveguide

Let us consider an infinite rectangular waveguide of dimensions a and b, as shown in Figure 2.1. The TEM field configuration cannot satisfy the boundary conditions for the waveguide walls [14], so only the TE and TM field configurations are valid solutions for the rectangular waveguide. The electric and magnetic fields in terms of the vector potentials **A** and **F** are given by [14]

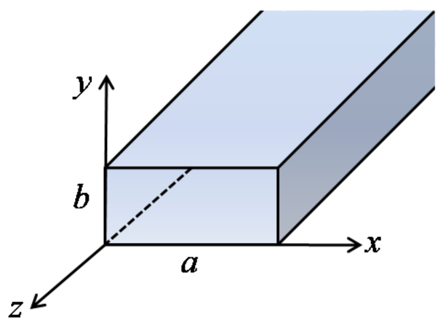

Figure 2.1: Infinite rectangular waveguide.

$$\mathbf{E} = \mathbf{E}_A + \mathbf{E}_F = -j\omega\mathbf{A} - j\frac{1}{\omega\mu\varepsilon}\nabla\left(\nabla\cdot\mathbf{A}\right) - \frac{1}{\varepsilon}\nabla\times\mathbf{F}, \tag{2.1}$$

$$\mathbf{H} = \mathbf{H}_A + \mathbf{H}_F = \frac{1}{\mu}\nabla\times\mathbf{A} - j\omega\mathbf{F} - j\frac{1}{\omega\mu\varepsilon}\nabla\left(\nabla\cdot\mathbf{F}\right), \tag{2.2}$$

where the vector potentials **A** and **F** have a solution of the form

$$\mathbf{A}\left(x,y,z\right) = \hat{a}_x A_x\left(x,y,z\right) + \hat{a}_y A_y\left(x,y,z\right) + \hat{a}_z A_z\left(x,y,z\right), \tag{2.3}$$

which satisfies

$$\nabla^2\mathbf{A} + \beta^2\mathbf{A} = 0, \tag{2.4}$$

and

$$\mathbf{F}\left(x,y,z\right) = \hat{a}_x F_x\left(x,y,z\right) + \hat{a}_y F_y\left(x,y,z\right) + \hat{a}_z F_z\left(x,y,z\right), \tag{2.5}$$

which satisfies

$$\nabla^2\mathbf{F} + \beta^2\mathbf{F} = 0. \tag{2.6}$$

We choose the TM and TE modes on the z direction, which we assume is the path of the traveling wave. Thus, we let the potential vectors **A** and **F** have only a component in the z direction

$$\mathbf{A}\left(x,y,z\right) = \hat{a}_z A_z\left(x,y,z\right), \tag{2.7}$$

and

$$\mathbf{F}\left(x,y,z\right) = \hat{a}_z F_z\left(x,y,z\right), \tag{2.8}$$

where A_z must satisfies the scalar wave equation

$$\nabla^2 A_z(x,y,z) + \beta^2 A_z(x,y,z) = \frac{\partial^2 A_z}{\partial x^2} + \frac{\partial^2 A_z}{\partial y^2} + \frac{\partial^2 A_z}{\partial z^2} + \beta^2 A_z = 0 \tag{2.9}$$

and F_z must satisfies

$$\nabla^2 F_z(x,y,z) + \beta^2 F_z(x,y,z) = \frac{\partial^2 F_z}{\partial x^2} + \frac{\partial^2 F_z}{\partial y^2} + \frac{\partial^2 F_z}{\partial z^2} + \beta^2 F_z = 0. \tag{2.10}$$

Using the separation of variables method, we assume that the solution for (2.9) can be written as

$$A_z(x,y,z) = f(x)\, g(y)\, h(z)\,. \tag{2.11}$$

Substituting (2.11) into (2.9) and dividing by fgh, we can write that

$$\frac{1}{f}\frac{d^2 f}{dx^2} + \frac{1}{g}\frac{d^2 g}{dy^2} + \frac{1}{h}\frac{d^2 h}{dz^2} = -\beta^2. \tag{2.12}$$

Each of the terms on the left is a function of only a single variable. Since their sum can only be equal to $-\beta^2$ if each term is a constant, we can rewrite (2.12) as three separate equations of the form

$$\begin{aligned} \frac{d^2 f}{dx^2} &= -\beta_x^2 f, \\ \frac{d^2 g}{dy^2} &= -\beta_y^2 g, \\ \frac{d^2 h}{dz^2} &= -\beta_z^2 h, \end{aligned} \tag{2.13}$$

where

$$\beta_x^2 + \beta_y^2 + \beta_z^2 = \beta^2 = \omega^2 \mu\varepsilon. \tag{2.14}$$

We can find the solutions for (2.13) in terms of complex exponentials (traveling waves) or in terms of cosine and sine (standing waves). In our case, the solutions for the equations in (2.13) can be written as

$$\begin{aligned} f(x) &= A\cos(\beta_x x) + B\sin(\beta_x x), \\ g(y) &= C\cos(\beta_y y) + D\sin(\beta_y y), \\ h(z) &= Ee^{-j\beta_z z} + Fe^{+j\beta_z z}. \end{aligned} \tag{2.15}$$

We have chosen the traveling waves solution for the function $h(z)$ since the waveguide is not bounded in the z direction. For the rectangular waveguide case, (2.11) can be rewritten as

$$\begin{aligned} A_z(x,y,z) = {} & [A\cos(\beta_x x) + B\sin(\beta_x x)]\,[C\cos(\beta_y y) + D\sin(\beta_y y)] \\ & \left[Ee^{-j\beta_z z} + Fe^{+j\beta_z z}\right], \end{aligned} \tag{2.16}$$

where $A, B, C, D, E, F, \beta_x, \beta_y$ and β_z are constants that can be computed by enforcing the appropriate boundary conditions on the $\mathbf{E}$ and $\mathbf{H}$ field components. By applying the same calculations, we can attain a similar solution for the potential $\mathbf{F}$.

2.2.2 Transverse Magnetic (TM) Modes

The TM modes are field configurations whose magnetic field components lie in a plane that is transverse to a given direction. Assuming $H_z = 0$ and $\mathbf{F} = 0$, we can easily derive the field expressions as [14]

$$
\begin{aligned}
E_x &= -j\frac{1}{\omega\mu\varepsilon}\frac{\partial^2 A_z}{\partial x \partial z} & H_x &= \frac{1}{\mu}\frac{\partial A_z}{\partial y} \\
E_y &= -j\frac{1}{\omega\mu\varepsilon}\frac{\partial^2 A_z}{\partial y \partial z} & H_y &= -\frac{1}{\mu}\frac{\partial A_z}{\partial x} \\
E_z &= -j\frac{1}{\omega\mu\varepsilon}\left(\frac{\partial^2}{\partial z^2}+\beta^2\right)A_z & H_z &= 0.
\end{aligned}
\tag{2.17}
$$

Using the separation of variables method, we can find the solution to (2.16). If we assume the wave is traveling only in the positive z direction, the second exponential of (2.16) becomes zero. Thus, we can write it as

$$
\begin{aligned}
A_z\left(x,y,z\right) = {} & \left[A\cos\left(\beta_x x\right)+B\sin\left(\beta_x x\right)\right]\left[C\cos\left(\beta_y y\right)+D\sin\left(\beta_y y\right)\right] \\
& Ee^{-j\beta_z z}.
\end{aligned}
\tag{2.18}
$$

The boundary conditions for the rectangular waveguide require the tangential components of the electric field to be zero on the walls of the waveguide. By enforcing the boundary conditions on the top and bottom walls, we can write that

$$
\begin{aligned}
E_x(0 \leqslant x \leqslant a, y=0, z) = E_x(0 \leqslant x \leqslant a, y=b, z) = 0, \\
E_z(0 \leqslant x \leqslant a, y=0, z) = E_z(0 \leqslant x \leqslant a, y=b, z) = 0,
\end{aligned}
\tag{2.19}
$$

and on the left and right walls

$$
\begin{aligned}
E_y(x=0, 0 \leqslant y \leqslant b, z) = E_y(x=a, 0 \leqslant y \leqslant b, z) = 0, \\
E_z(x=0, 0 \leqslant y \leqslant b, z) = E_z(x=a, 0 \leqslant y \leqslant b, z) = 0.
\end{aligned}
\tag{2.20}
$$

Substituting (2.18) into (2.17) and applying the boundary conditions (2.19) and (2.20), we attain that

$$E_x(0 \leq x \leq a, y = 0, z) = 0 \Leftrightarrow C = 0 \tag{2.21}$$
$$E_x(0 \leq x \leq a, y = b, z) = 0 \Leftrightarrow \sin(\beta_y b) = 0 \Leftrightarrow \beta_y b = n\pi \Leftrightarrow \beta_y = \frac{n\pi}{b}$$
$$n = 1, 2, 3, ...$$

and

$$E_y(x = 0, 0 \leqslant y \leqslant b, z) = 0 \Leftrightarrow A = 0, \tag{2.22}$$
$$E_y(x = a, 0 \leqslant y \leqslant b, z) = 0 \Leftrightarrow \sin(\beta_x a) = 0 \Leftrightarrow \beta_x a = m\pi \Leftrightarrow \beta_x = \frac{m\pi}{a}$$
$$n = 1, 2, 3, ...$$

So (2.18) is reduced to

$$\begin{aligned} A_z(x, y, z) &= BDE\left[\sin\left(\frac{m\pi}{a}x\right)\sin\left(\frac{n\pi}{b}y\right)\right]e^{-j\beta_z z} \\ &= A_{mn}\left[\sin\left(\frac{m\pi}{a}x\right)\sin\left(\frac{n\pi}{b}y\right)\right]e^{-j\beta_z z}. \end{aligned} \tag{2.23}$$

Hence, we can write the field expressions (2.17) for the TM^z field configurations as

$$\begin{aligned} E_x &= -A_{mn}\frac{\beta_x\beta_z}{\omega\mu\varepsilon}\cos(\beta_x x)\sin(\beta_y y)e^{-j\beta_z z} \\ H_x &= A_{mn}\frac{\beta_y}{\mu}\sin(\beta_x x)\cos(\beta_y y)e^{-j\beta_z z} \\ E_y &= -A_{mn}\frac{\beta_y\beta_z}{\omega\mu\varepsilon}\sin(\beta_x x)\cos(\beta_y y)e^{-j\beta_z z} \\ H_y &= -A_{mn}\frac{\beta_x}{\mu}\cos(\beta_x x)\sin(\beta_y y)e^{-j\beta_z z} \\ E_z &= -jA_{mn}\frac{\beta_c^2}{\omega\mu\varepsilon}\sin(\beta_x x)\sin(\beta_y y)e^{-j\beta_z z} \\ H_z &= 0, \end{aligned} \tag{2.24}$$

where

$$\beta_c^2 \equiv \left(\frac{2\pi}{\lambda_c}\right)^2 = \beta^2 - \beta_z^2 = \beta_x^2 + \beta_y^2 = \left(\frac{m\pi}{a}\right)^2 + \left(\frac{n\pi}{b}\right)^2. \quad (2.25)$$

The constant β_c is called the *cut off wave number* and is the value of β when β_z is equal to zero,

$$\beta_c = \beta|_{\beta_z=0} = \omega\sqrt{\mu\varepsilon}|_{\beta_z=0} = \omega_c\sqrt{\mu\varepsilon} = 2\pi f_c\sqrt{\mu\varepsilon} = \sqrt{\left(\frac{m\pi}{a}\right)^2 + \left(\frac{n\pi}{b}\right)^2}. \quad (2.26)$$

From (2.26), we can write the expression for the *cut off frequency* for a given mn mode as

$$(f_c)_{mn} = \frac{1}{2\pi\sqrt{\mu\varepsilon}}\sqrt{\left(\frac{m\pi}{a}\right)^2 + \left(\frac{n\pi}{b}\right)^2}. \quad (2.27)$$

When the frequency of operation is smaller than the *cut off frequency* (for a given mn mode), there are not propagating waves and the fields are attenuated. However, when the frequency is higher than the $(f_c)_{mn}$, we have propagating waves and the fields are unattenuated [14].

2.2.3 Transverse Electric (TE) Modes

The TE modes are field configurations where the electric field lies in a plane that is transverse to a given direction. By choosing the z direction as path of the travelling wave, we have $E_z = 0$ and $\mathbf{A} = 0$. Moreover, the field components can be written as

$$\begin{aligned}
E_x &= -\frac{1}{\varepsilon}\frac{\partial F_z}{\partial y} & H_x &= -j\frac{1}{\omega\mu\varepsilon}\frac{\partial^2 F_z}{\partial x \partial z} \\
E_y &= \frac{1}{\varepsilon}\frac{\partial F_z}{\partial x} & H_y &= -j\frac{1}{\omega\mu}\frac{\partial^2 F_z}{\partial y \partial z} \\
E_z &= 0 & H_z &= -j\frac{1}{\omega\mu\varepsilon}\left(\frac{\partial^2}{\partial z^2} + \beta^2\right) F_z.
\end{aligned} \tag{2.28}$$

Using the separation of variables method, we can find a similar solution for the potential **F** as the one obtained for the potential **A** in (2.18). Then, by satisfying the boundary conditions (2.19) and (2.20), we can write

$$\begin{aligned}
F_z\left(x, y, z\right) &= B_{mn} \cos\left(\beta_x x\right) \cos\left(\beta_y y\right) e^{-j\beta_z z} \\
&= B_{mn}\left[\cos\left(\frac{m\pi}{a}x\right)\cos\left(\frac{n\pi}{b}y\right)\right] e^{-j\beta_z z},
\end{aligned} \tag{2.29}$$

where

$$\begin{aligned}
\beta_x &= \frac{m\pi}{a} & m &= 0, 1, 2, ... \\
\beta_y &= \frac{n\pi}{b} & n &= 0, 1, 2, ...
\end{aligned} \tag{2.30}$$

So, the final expressions for the fields are

$$\begin{aligned}
E_x &= -A_{mn}\frac{\beta_x\beta_z}{\omega\mu\varepsilon}\cos(\beta_x x)\sin(\beta_y y)e^{-j\beta_z z} \\
H_x &= B_{mn}\frac{\beta_x\beta_z}{\omega\mu\varepsilon}\sin(\beta_x x)\cos(\beta_y y)e^{-j\beta_z z} \\
E_y &= -B_{mn}\frac{\beta_x}{\varepsilon}\sin(\beta_x x)\cos(\beta_y y)e^{-j\beta_z z} \\
H_y &= B_{mn}\frac{\beta_y\beta_z}{\omega\mu\varepsilon}\cos(\beta_x x)\sin(\beta_y y)e^{-j\beta_z z} \\
E_z &= 0 \\
H_z &= -jB_{mn}\frac{\beta_c^2}{\omega\mu\varepsilon}\cos(\beta_x x)\cos(\beta_y y)e^{-j\beta_z z},
\end{aligned} \tag{2.31}$$

where $\beta_c^2 = \left(\frac{m\pi}{a}\right)^2 + \left(\frac{n\pi}{b}\right)^2$ is the *cut off wave number*.

2.2.4 Rectangular Resonant Cavity

A rectangular cavity is formed by enclosing the front and back section of a waveguide with conducting plates, as shown in Figure 2.2. The field configurations inside the cavity can be either TE or TM. Considering first the TM modes and the z direction as the direction of the propagation path, we can find the expressions for the configuration fields as done before. We can attain a similar solution for the potential **A** as in (2.16) and (2.23)

$$\begin{aligned} A_z(x,y,z) &= [A\cos(\beta_x x) + B\sin(\beta_x x)]\,[C\cos(\beta_y y) + D\sin(\beta_y y)] \\ &\quad [E\cos(\beta_z z) + F\sin(\beta_z z)]\,, \\ &= A_{mn}\sin(\beta_x x)\sin(\beta_y y)\,[E\cos(\beta_z z) + F\sin(\beta_z z)]\,. \end{aligned} \tag{2.32}$$

By applying the additional boundary condition on the front and the back sides

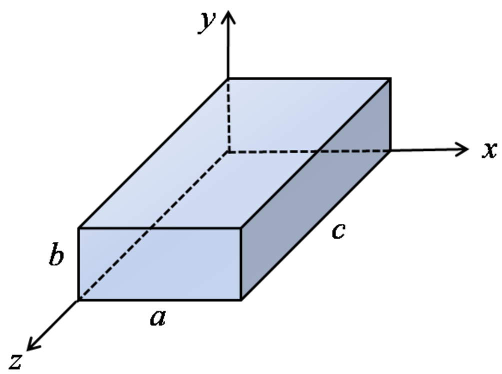

Figure 2.2: Rectangular resonant cavity.

of the cavity, we can find that (2.32) is reduced to

$$A_z(x,y,z) = A_{mnp} \sin(\beta_x x) \sin(\beta_y y) \cos(\beta_z z), \tag{2.33}$$

where

$$\begin{aligned} \beta_x &= \frac{m\pi}{a} \qquad m = 1, 2, 3, ... \\ \beta_y &= \frac{n\pi}{b} \qquad n = 1, 2, 3, ... \\ \beta_z &= \frac{p\pi}{c} \qquad p = 0, 1, 2, ... \end{aligned} \tag{2.34}$$

Each combination of these m, n and p represents one mode and the modes are only present when

$$\beta_c^2 = \omega_c^2 \mu\varepsilon = (2\pi f_c)^2 \mu\varepsilon = \beta_x^2 + \beta_y^2 + \beta_z^2 = \left(\frac{m\pi}{a}\right)^2 + \left(\frac{n\pi}{b}\right)^2 + \left(\frac{p\pi}{c}\right)^2, \tag{2.35}$$

and

$$(f_c)_{mnp} = \frac{1}{2\pi\sqrt{\mu\varepsilon}} \sqrt{\left(\frac{m\pi}{a}\right)^2 + \left(\frac{n\pi}{b}\right)^2 + \left(\frac{p\pi}{c}\right)^2}. \tag{2.36}$$

In a similar way, we can find the TE solutions that satisfy the boundary conditions. Thus, we can write that

$$F_z(x,y,z) = B_{mnp} \cos(\beta_x x) \cos(\beta_y y) \sin(\beta_z z), \tag{2.37}$$

where

$$\begin{aligned} \beta_x &= \frac{m\pi}{a} \qquad m = 0, 1, 2, ... \\ \beta_y &= \frac{n\pi}{b} \qquad n = 0, 1, 2, ... \\ \beta_z &= \frac{p\pi}{c} \qquad p = 1, 2, 3, ... \end{aligned} \tag{2.38}$$

and the resonant frequency is defined in (2.36).

2.2.5 Modal Description of a Reverberation Chamber

The rectangular resonant cavity is the best approximation of a real reverberation chamber. Thus, the field inside a RC can be described as resonant modes. When the chamber is empty, the modes inside can be expressed through (2.33) for the TM case and (2.37) for the TE case. Considering the TE solutions, we can express the sine and cosine in (2.37) in terms of exponentials as

$$\begin{aligned}F_z\left(x,y,z\right) =& B_{mnp}\cdot\frac{e^{i\beta_x x}+e^{-i\beta_x x}}{2}\cdot\frac{e^{i\beta_y y}+e^{-i\beta_y y}}{2}\cdot\frac{e^{i\beta_z z}-e^{-i\beta_z z}}{2i}, \\ =&\mathrm{Const}\cdot\left(e^{i\beta_x x+i\beta_y y+i\beta_z z}+e^{i\beta_x x-i\beta_y y+i\beta_z z}+e^{-i\beta_x x+i\beta_y y+i\beta_z z}+e^{-i\beta_x x-i\beta_y y+i\beta_z z}+\right.\\ &\left.-e^{-i\beta_x x+i\beta_y y-i\beta_z z}-e^{i\beta_x x-i\beta_y y-i\beta_z z}-e^{-i\beta_x x+i\beta_y y-i\beta_z z}-e^{-i\beta_x x-i\beta_y y-i\beta_z z}\right)\\ =&\mathrm{Const}\cdot\sum_1^8 e^{\pm i\beta_x x\pm i\beta_y y\pm i\beta_z z}=\mathrm{Const}\cdot\sum_1^8 \mathrm{e}^{-\mathrm{i}\boldsymbol{\beta}\cdot\mathbf{r}},\end{aligned} \tag{2.39}$$

where $\mathbf{r}=x\hat{x}+y\hat{y}+z\hat{z}$ and $\boldsymbol{\beta}=\beta_x\hat{x}+\beta_y\hat{y}+\beta_z\hat{z}$ with $\beta_x=\mp\frac{m\pi}{a}$, $\beta_y=\mp\frac{n\pi}{b}$ and $\beta_z=\mp\frac{p\pi}{c}$. From (2.39), we can see that each mode is represented as a sum of eight plane waves for both the TE and TM modes, except for the cases when one of the indexes is zero, in which the plane waves are four. Each of the eight terms in (2.39), represents a plane wave propagating in one of the eight directions defined by $\boldsymbol{\beta}=\beta_x\hat{x}+\beta_y\hat{y}+\beta_z\hat{z}$. Theoretically, for a lossless cavity, a mode can be excited only when the excitation frequency is exactly equal to the resonance frequency of the mode. In reality, some losses are always present in cavities, and in particular for chambers when lossy objects are placed in them. Then, modes can be excited in a certain mode bandwidth Δf and all the resonances within the range $f_{mnp}-\Delta f/2\leq f\leq f_{mnp}+\Delta f/2$ will be excited by the frequency f, as shown in Figure 2.3. We can also excite more resonances when we use stirring methods [15]. When the modes are stirred, the resonant frequencies will shift and more modes can be excited at a given frequency.

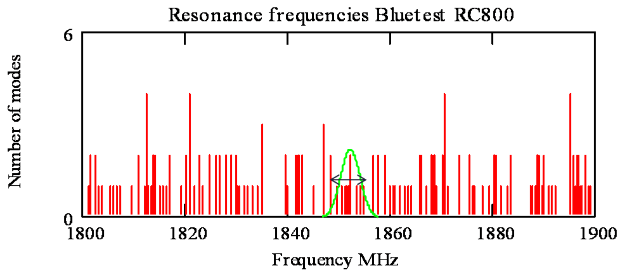

Figure 2.3: Number of modes excited within the mode bandwidth [16].

2.3 Reverberation Chamber Geometry

The geometry of a reverberation chamber is illustrated in Figure 2.4. The chamber consists of three mechanical stirrers, two plates on the wall sides and one platform. A polarization stirring is activated by mounting three wall antennas on three orthogonal walls. A further stirring method, called frequency stirring is used during the post-processing of the data. The transmission coefficient S_{21} is measured between two antennas in the chamber. One is the antenna under test (AUT) and the other one is a wall antenna and it is part of the chamber. The chamber is powered using a transmitting antenna, the wall antenna, connected (via a mechanical switch) to a Vector Network Analyzer (VNA) acting as a source. The receiving antenna (AUT) is connected to another port of the VNA and the received power is measured via S_{21}.

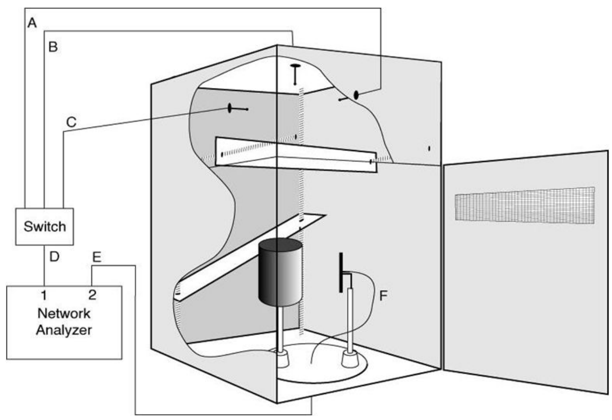

Figure 2.4: Schematic view of the Reverberation Chamber.

2.3.1 Lossy Objects

The resonant modes excited inside the reverberation chamber are characterized by their bandwidths and the resonant frequencies. The bandwidth depends on how much the chamber is loaded [17] and the resonance frequencies change as we move the stirrers inside the chamber. When we load the chamber, the mode bandwidth increases such that more modes can be excited ensuring a uniform distribution of plane waves. Moreover, on the measurement of active terminals, we need a Δf larger than the modulation bandwidth of the channel in order to avoid measurements errors and distortions in the modulation. When we use a mobile phone, the antenna is typically close to lossy objects, like our head or hands. Therefore, on the measurement of a mobile terminal in the chamber, we need to put inside some lossy objects, e.g., a head phantom or/and a lossy cylinder, to ensure that we are measuring in the same conditions of the real environment.

2.3.2 Stirring Methods

The stirring methods are used to create a large overmoded cavity in which the field is continuously perturbed by shifting the eigenfrequency of the resonant modes [15] in order to achieve a rich scattering environment with a uniform random field. The stirring methods are three: mechanical (plates + platform), polarization and frequency stirring.

Plates Stirring

The mechanical stirrers are two metallic plates on the side walls of the chamber and a rotating platform. The plates move along the walls in order to shift the resonant frequency of the excited modes. When the plates move, the excited modes within Δf shift, so that an additional bandwidth will be added to the Δf, increasing the total mode bandwidth and ensuring more excited modes [16]. In figure 2.5 are shown the mechanical plates in the Bluetest RC at Chalmers University of Technology. It has one 15×140 cm metallic plate on the front wall and one 100×15 cm on the left wall. They move orthogonally between each other and their dimensions should be at least two wavelengths in order to achieve a proper stirring [15].

Figure 2.5: Mechanical plates in the RC at Chalmers University of Technology.

Platform Stirring

In the platform stirring process, the AUT is located on a rotating platform inside the chamber, as shown in Figure 2.6. While the platform rotates, the AUT sees new different scenarios for each platform position. Thus, when the antenna is in a new position, we have a different mode distribution compared to the one on the previous step and consequently we achieve more independent modes [5]. Moreover, for each position, the plane waves will arrive from different directions on the AUT ensuring a uniform distribution of the field inside the chamber.

Moving the AUT, we can also remove the direct coupling between the AUT and the excitation antenna (wall-fixed antenna), that can affect the Rayleigh distribution of the field.

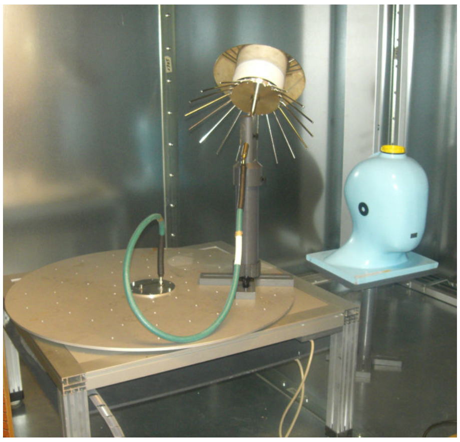

Figure 2.6: Platform stirrer in the RC at Chalmers University of Technology.

Polarization Stirring

Instead of using one fixed excitation antenna, we excite the chamber with three orthogonally linearly polarized antennas, mounted on three different walls of the chamber. The antenna under test sees different polarizations of the waves contributing to create an isotropic multipath environment inside the chamber. The orthogonal placement of the antennas ensures that all the polarizations get equally importance and it can also reduce the polarization imbalance. Several investigations [6] have shown that the received power level depends on the orientation of the AUT when only one excitation antenna is used. This phenomenon is called polarization imbalance and it can affect the uniformity of the field inside the chamber. However, it can be strongly reduced by using three orthogonally excitation antennas instead of one and then taking the average of the chamber transfer function (see section 3.2) over all the three antennas. In Figure 2.7 is shown one of the fixed wall antennas in the RC at Chalmers University of Technology.

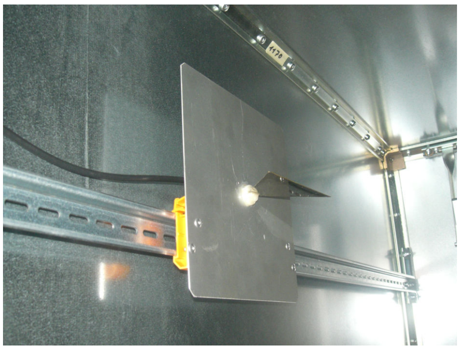

Figure 2.7: One wall antenna in the RC at Chalmers University of Technology.

Frequency Stirring

The frequency stirring method is used during the data processing. It consists in processing the data at a certain frequency f considering also the information of the neighboring frequency points within a chosen bandwidth, called frequency stirring bandwidth. In the data processing, the transmissions at those frequency points will be averaged and presented as the transmission of the single frequency point f, in which we performed our measurement. For instance, assume that we want to measure the single frequency 1800 MHz and we choose a frequency stirring bandwidth $B_{FS} = 4$ MHz. Thus, the VNA will not only measure the transmission at 1800 MHz, but also $B_{FS}/2$ frequency points on each side of the chosen frequency point will be added. It means that the VNA will measure the samples relative to the frequencies 1798, 1799, 1800, 1801 and 1802 MHz. Then, in the data processing, the transmissions at all these points will be averaged and presented as the transmission of the one single frequency point at 1800 MHz. By using the frequency stirring we attain a better accuracy, but the disadvantage of using this technique is that the frequency resolution of the measurements will decrease, and it makes difficult to resolve variations in the measurements that are lower than the frequency stirring bandwidth.

2.4 Statistical Distribution of the Field

The field inside the chamber is continuously perturbed and stirred causing the transmitted signal to be reflected many times by the walls before reaching the receiving antenna. Due to this phenomenon, several signals will arrive to the receiving antenna with random phases, so that the field inside the chamber has a statistical behavior. The E-field is the vector sum of three components and each of them consists of a real and imaginary part. Hence, the E field can be written as

$$\mathbf{E} = \mathbf{E}_x + \mathbf{E}_y + \mathbf{E}_z, \tag{2.40}$$

where

$$\mathbf{E}_{x,y,z} = \mathrm{Re}\left(\mathbf{E}_{x,y,z}\right) + j\mathrm{Im}\left(\mathbf{E}_{x,y,z}\right). \tag{2.41}$$

Since the field is strongly stirred, each of these components is represented as the sum of many uncorrelated multipath waves coming from different directions in the chamber. Thus, as the central limit theorem states, each real and imaginary part is normally distributed with zero mean and variance σ^2 and each multipath wave becomes an independent random variable [18]. The magnitude of the field $|\mathbf{E}_{x,y,z}|$ is chi-square distributed and has a probability density function (pdf)

$$f\left(|\mathbf{E}_{x,y,z}|\right) = \frac{|\mathbf{E}_{x,y,z}|}{\sigma^2}\exp\left(-\frac{|\mathbf{E}_{x,y,z}|^2}{2\sigma^2}\right). \tag{2.42}$$

The received power, that is proportional to the square of the magnitude of the field, has an exponential pdf defined by

$$f\left(|\mathbf{E}_{x,y,z}|^2\right) = \frac{1}{2\sigma^2}\exp\left(-\frac{|\mathbf{E}_{x,y,z}|^2}{2\sigma^2}\right). \tag{2.43}$$

These are the characteristic of a Rayleigh fading model. As shown in Figure 2.8, the received complex signal S_{21} obtained from the measured data, is Gaussian complex distributed and its magnitude has a Rayleigh distribution [16]. In Figure

2.9, it is shown the typical cumulative distribution function (cdf) of a Rayleigh fading signal normalized to the signal amplitude for each wall antenna. For these reasons, the reverberation chamber can emulate a Rayleigh fading environment with a field that is uniformly distributed when it is averaged over a sufficient number of independent signal transmissions (samples) [19]. In figure 2.10, we can see the propagation directions of the plane waves in the chamber. They are uniformly distributed over the whole unit sphere.

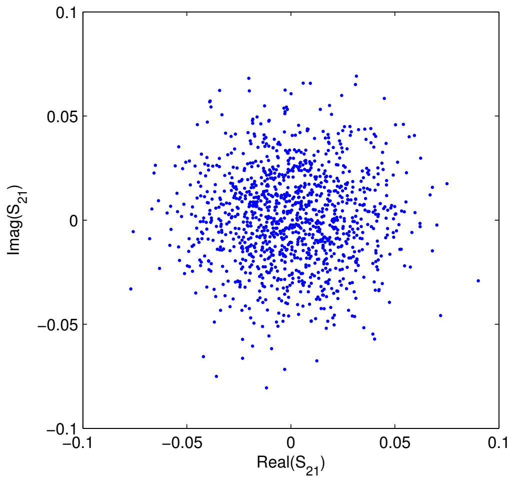

Figure 2.8: Normal distribution of the real and imaginary parts of the transmission coefficient S_{21}.

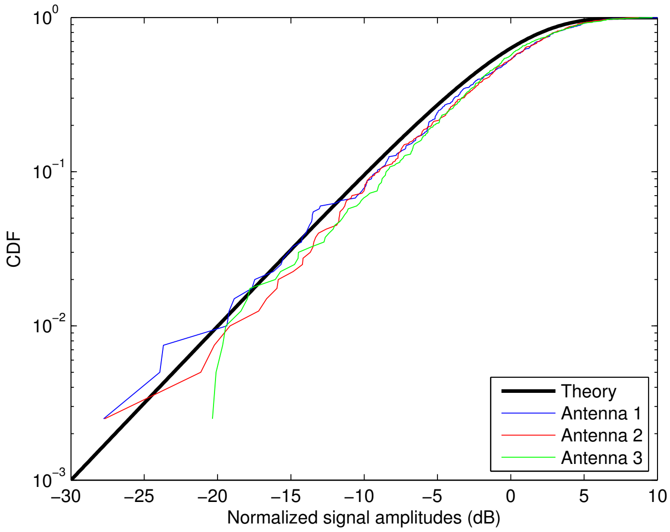

Figure 2.9: Cumulative distribution function of the signal amplitude. The black curve is the theory and the color curves are the measurements for each wall antenna.

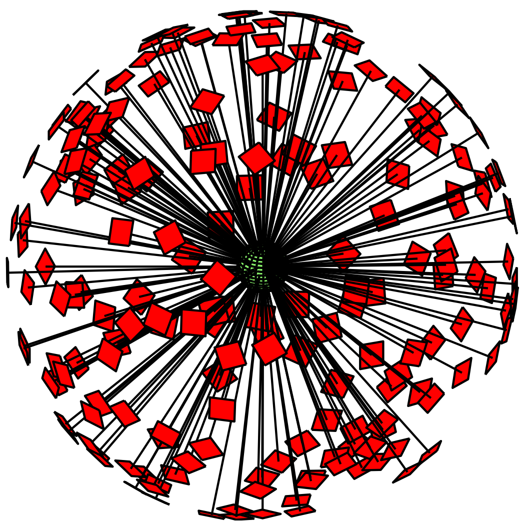

Figure 2.10: Propagation directions of the plane waves over the whole unit sphere.

Chapter 3

Measurements Setup

3.1 Bluetest High Performance Reverberation Chamber

In Figure 3.1 is shown an overview of the RC at Chalmers University of Technology. The new chamber with the following dimensions 1.25 × 1.85 × 1.75 m has a volume of 4 m^3 and a shielding effectiveness of 100 dB. It works in a wide frequency range between 0.7-6 GHz (recommended frequency range) and the speed of the stirrers is increased, ensuring shorter measurement time. For an active measurement, the device under test (DUT) is located on the platform and a communication tester is used to setup a call with the DUT. Then, the relative output power is sampled by the wall antennas. In a passive measurement, in which the port 1 of the VNA is connected to the wall antennas (through a mechanical switch) and the port 2 to the antenna under test, the S-parameters between the two antennas are measured. The measured data, called raw data, are collected by the network analyzer that is connected to a monitoring computer. All the measurements setup is monitored by the Bluetest software predefined in the computer. Then, the collected raw data are processed using Matlab programs.

Figure 3.1: Overview of the Reverberation Chamber at Chalmers University of Technology.

3.2 Measured Parameters

When a measurement is started up, the S-parameters between the wall antenna, transmitting antenna, and the AUT, receiving antenna, are measured, as shown in Figure 3.2. In this Figure, we can observe that S_{11} is the reflection coefficient of the wall antennas, S_{22} is the return loss of the antenna under test, and S_{21} is the transmission coefficient between the excitation antenna and the receiving antenna. The received power is achieved by calculating the chamber transfer function (or power transfer function) that can be described as

$$G_{\text{chamber}} = \frac{1}{N}\sum_{n=1}^{N}\frac{|S_{21}^{n}|^2}{\left(1-|\overline{S_{11}}|^2\right)\left(1-|\overline{S_{22}}|^2\right)}, \tag{3.1}$$

where the numerator is the received power averaged over all the stirrer positions. The role of the denominator is to exclude the return loss of the antennas from the transfer function, where $\overline{S_{11}}$ and $\overline{S_{22}}$ denote the complex averaging over all the stirrer positions.

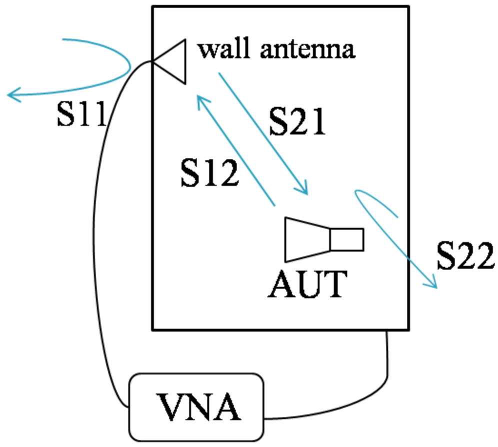

Figure 3.2: Schematic view of the measured parameters in the RC.

3.2.1 Free Space Parameters

The average values of the reflection coefficient and of the return loss defined in (3.1) give the same values of S_{11} and S_{22} that would be measured in free space [20], since each of them can be written as the sum of a deterministic free space part plus an incoming part from the chamber. This last part is statistic and complex Gaussian distributed with zero mean

$$S_{11} = S_{11}^{\mathrm{Free-space}} + S_{11}^{\mathrm{Chamber}}, \tag{3.2}$$

$$S_{22} = S_{22}^{\mathrm{Free-space}} + S_{22}^{\mathrm{Chamber}}. \tag{3.3}$$

This means that the expected mean over all the stirrer positions in the chamber is zero. Then, if we evaluate the mean of the total complex reflection coefficient and return loss, it will be equal to the components on the free space

$$\overline{S_{11}} = \frac{1}{N}\sum_{n=1}^{N} S_{11}^{n} = S_{11}^{\mathrm{Free-Space}}, \tag{3.4}$$

$$\overline{S_{22}} = \frac{1}{N}\sum_{n=1}^{N} S_{22}^{n} = S_{22}^{\mathrm{Free-Space}}. \tag{3.5}$$

For these reasons, the transmission coefficient S_{21} can be defined as the sum of two contributions, one deterministic and unstirred, the same as in the free space, and one that is statistical, stirred and comes from the chamber. To ensure that the RC provides an isotropic reference environment with a Rayleigh fading, the direct coupling between the receiving and the transmitting antennas should be as small as possible. It follows the Friis's formula [21], used to compute the transmission between two antennas in the free space, i.e.,

$$\left|S_{21}^{\mathrm{Free-Space}}\right|^2 = \left(\frac{\lambda}{4\pi r}\right)^2 G_t G_r. \tag{3.6}$$

where λ is the wavelength, r is the distance between the two antennas and G_t and G_r are the gains of the transmitting and receiving antennas, respectively. The direct coupling can be used to get a Rician distribution, but when the RC has to provide a Rayleigh fading environment, the direct coupling has to be smaller than the statistical contribution of the S_{21} and this can be done by a suitable platform and polarization stirring.

3.2.2 Transmission between two Antennas inside the RC and Losses Contributions

The transmission between two antennas in the chamber follows Hill's transmission formula [17]

$$G_{\mathrm{chamber}} = \frac{P_r}{P_t} = \frac{c^3 e_{\mathrm{tot.rad1}} e_{\mathrm{tot.rad2}}}{16\pi^2 V f^2 \Delta f}, \tag{3.7}$$

where $e_{\mathrm{tot.rad1}}$ is the total radiation efficiency of the wall antenna (transmitting antenna) and $e_{\mathrm{tot.rad2}}$ is the total radiation efficiency of the AUT (receiving antenna) including the mismatch of the two antennas, V is the chamber volume, and Δf is the average mode bandwidth. The Hill's formula varies with the frequency and it can be affected by the average mode bandwidth, which considers the losses in the chamber. The mode bandwidth is related to the Q factor [22] by

$Q = f/\Delta f$. The Q factor is also defined as the ratio between the stored energy $\mathrm{U_s}$ and the dissipated power $\mathrm{P_d}$ in the chamber [17], i.e.,

$$Q = 2\pi f \frac{U_s}{P_d}. \tag{3.8}$$

The dissipated power can be written as the sum of four terms: the losses due to the receiving antenna, objects inside the chamber, aperture leakage and non perfect conductivity in the chamber walls

$$P_d = P_{\text{wall}} + P_{\text{object}} + P_{\text{leakage}} + P_{\text{antenna}}. \tag{3.9}$$

Thus, we can write that

$$\frac{1}{Q} = \frac{P_d}{2\pi f U_s} = \frac{1}{Q_{\text{wall}}} + \frac{1}{Q_{\text{object}}} + \frac{1}{Q_{\text{leakage}}} + \frac{1}{Q_{\text{antenna}}}, \tag{3.10}$$

and

$$\Delta f = \Delta f_{\text{wall}} + \Delta f_{\text{object}} + \Delta f_{\text{leakage}} + \Delta f_{\text{antenna}}. \tag{3.11}$$

It can be shown [17] that

$$\Delta f_{\text{wall}} = \frac{2A}{3V}\sqrt{\frac{c\rho f}{\pi\eta}}, \tag{3.12}$$

$$\Delta f_{\text{object}} = \frac{c}{2\pi V}\sigma_a, \tag{3.13}$$

$$\Delta f_{\text{leakage}} = \frac{c}{4\pi V}\sigma_l, \tag{3.14}$$

$$\Delta f_{\text{antenna}} = \frac{c^3 e_{\text{rad}}}{16\pi^2 V f^2}, \tag{3.15}$$

where V is the volume of the chamber, c is the speed of the light, ρ is the resistivity of the material of the chamber, A is the surface area, η is the free space wave impedance, σ_a is the average absorption cross section of the lossy object,

σ_l is the average transmission cross section of the apertures in the chamber and e_{rad} is the radiation efficiency of the receiving antenna. In Figure 3.3 are shown the different loss contributions on the total mode bandwidth. It can be seen that when a lossy object is present in the chamber, the mode bandwidth increases. Instead, the losses due to the walls are usually negligible (less than 0.1 MHz).

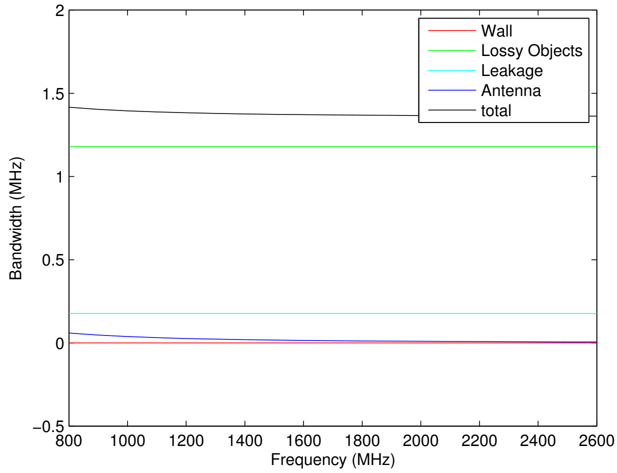

Figure 3.3: Different losses contributions that affect the mode bandwidth. The loss contributions are plotted considering the dimensions of the RC at Chalmers University of Technology.

3.2.3 Test Case and Reference Case

Since the chamber transfer function is proportional to the total radiation efficiency of an antenna (as can be seen in (3.7)), we can easily compute the chamber transfer function of the AUT from the measured S-parameters and then extract the relative radiation efficiency. A comparison of the efficiency of different antennas can be done by measuring them one by one and then comparing their transfer functions. An absolute value of the total radiation efficiency is obtained by comparing the chamber transfer function of an AUT with the chamber transfer function of an antenna with known radiation efficiency. Such antenna is referred to as a reference antenna. Thus, the first step is to measure the transfer function of the reference antenna (done during the calibration procedure of the chamber) as

$$P_{\text{ref}} = \frac{1}{N} \sum_{n=1}^{N} \frac{\left|S_{12,\text{ref}}^{n}\right|^{2}}{\left(1 - \left|\overline{S_{11}}\right|^{2}\right)\left(1 - \left|\overline{S_{22,\text{ref}}}\right|^{2}\right)}. \tag{3.16}$$

In this case, the total radiation efficiency $e_{\text{tot.rad2}}$ of the reference antenna is already known and the $e_{\text{tot.rad1}}$ of the wall antennas does not need to be known since it will be the same for both reference and test measurements. As a second step, the AUT is measured and its transfer function is determinate as

$$P_{\text{AUT}} = \frac{1}{N} \sum_{n=1}^{N} \frac{\left|S_{12,\text{AUT}}^{n}\right|^{2}}{\left(1 - \left|\overline{S_{11}}\right|^{2}\right)\left(1 - \left|\overline{S_{22,\text{AUT}}}\right|^{2}\right)}. \tag{3.17}$$

Then, the ratio between the two average transfer functions will be equal to the ratio between the radiation efficiencies of the AUT and the reference antenna. We can easily get the absolute value of the total radiation efficiency for the AUT as

$$e_{\text{tot.rad}} = \frac{P_{\text{AUT}}}{P_{\text{ref}}} \left(1 - \left|\overline{S_{22,\text{AUT}}}\right|^{2}\right), \tag{3.18}$$

$$e_{\text{rad}} = \frac{P_{\text{AUT}}}{P_{\text{ref}}}, \tag{3.19}$$

where $e_{\text{tot.rad}}$ is the total radiation efficiency of the AUT including the mismatch factor, and e_{rad} is simply the radiation efficiency of the AUT. Since the power level will change with the loading, the reference measurement must have the same loading as the test one. It means that if a different antenna is used for the reference case instead to the one used for the test case, both antennas have to be present in the chamber when a measurement is performed. To fulfill the boundary conditions, it is important that the AUT is not located closer than 0.5 wavelengths from any metal object and it should have a distance no less than 0.7 wavelengths from any lossy objects in order to perform a free space measurement.

3.3 Calibration Procedure

In order to calculate an absolute value for the radiated power of the test case, we need to do a calibration measurement of the average power level using a reference antenna with well known radiation characteristics. This is done by measuring the transmission between the reference antenna and the fixed wall antennas. Typically a broadband antenna is used as a reference antenna; in our case we used a disk-cone antenna working between 0.5 and 6 GHz. As explained in the previous section, the loading has to be the same for both test and reference measurements. Thus, one separate calibration measurement is needed for each different loading case. During a calibration procedure, cable losses and mismatch of the wall antennas are first determined. Then, the chamber transfer function of the reference antenna is measured with the AUT present inside the chamber and terminated with a matched port. It is also possible to calibrate the chamber without having the AUT inside. However, the reference antenna must be removed when the AUT is measured. As an advantage, we can use the same calibration on the measuring of several AUTs or many active terminals. Nevertheless, we can use this kind of calibration procedure only when the chamber is enough loaded so that the reference antenna and the AUT do not give any more contributions to the chamber mode bandwidth [21].

3.4 Bluetest Software

Each measurement settings is controlled and monitored by the Bluetest software. For calibration measurements, we use the *Bluetest reference* software. In Figure 3.4, we can see the main window that gives access to all the program settings. In the right area, there are all the bottoms to setup a reference measurement. The frequency editor, which is opened by pressing the frequencies bottom, is shown in Figure 3.5 and it is used to adjust the frequency settings that will be used by the VNA. The frequency list on the left column shows the frequency points that will be measured. The frequency points can be added to this list either by using the preset frequency points divided in different common frequency bands or by adding a range of frequency points defined by the start, step and stop bottoms. A frequency step of 1 MHz is usually used. Since the VNA cannot memorize more than 1500 frequency points per measurement, we usually measure in a frequency range no bigger than 1.5 GHz. As shown in Figure 3.5, we can also perform a single frequency point measurement. The frequency stirring setting affects the VNA as well as the data processing. Let us assume that we are measuring in a frequency range of 1 GHz as indicated in Figure. When we choose a frequency stirring of 10 MHz, the VNA will measure also the transmissions of the first ten neighboring frequency points, so that we have 1011 points instead of 1001. Then, during the data processing the transmissions of these ten frequency points will be averaged. We can also choose between two types of stirring sequences: continuous or stepped. In the continuous, the S-parameters will be sampled with a chosen sampling rate while the mode stirrers are moving continuously. In the stepped, the stirring mode will stop each time before measuring the S-parameters. Each of the called samples, correspond to an S parameter measurement in one frequency point. In our case, we used the stepped sequence. Thus, by pressing the config. bottom in the main window, we get access to the stepped stirring setting, as shown in Figure 3.6. We can choose the number of samples between three sequences, varying from 150 (with a shorter measurement time and accuracy) to 1200 (bigger measurement time but very accurate). For instance, if we choose a very accurate stepped mode sequence, the monitoring computer will collect 400 samples for each wall antenna, since the VNA measures the S-parameters simultaneously for each of the three wall antennas in each frequency point. Here is shown the typical file format that is saved from a reference measurement. In the first column are the frequencies in Hz, in the second, third and fourth columns are the transmissions in decimal form for each wall antenna, and in the fifth, sixth and seventh columns are the reflection coefficients for each wall antenna:

```
% Bluetest_ref
% file_ver 1.0
% 2008-04-05 19:08:17
% Raw data: Bluetest_raw/20080405-1908-6245.s
% NF: 1001
% NA: 3
% F[Hz], T[power], R[ampl]
1000000000   0.0102795550545568   0.347465473835386
```

```
0.0156706205252293
   0.0287577071368595    0.0126947309029056    0.189639375360336
1001000000   0.0103074567619455   0.353140296991137
0.015486438787491
   0.0550346941183146    0.0128568114750405    0.203243234504193
1002000000   0.010273399235536    0.361880882492912
0.0153231314987868
   0.0861574767919497    0.0129849798941502    0.214330025836372
1003000000   0.0102967371356698   0.37326214917374
0.0151686606022554
   0.118112975247685     0.0131496615376424    0.222449713311545
1004000000   0.0104267365437647   0.379184110482339
0.014937026717111
   0.145337973930087     0.0132320241733272    0.231774892324883
....
....
```

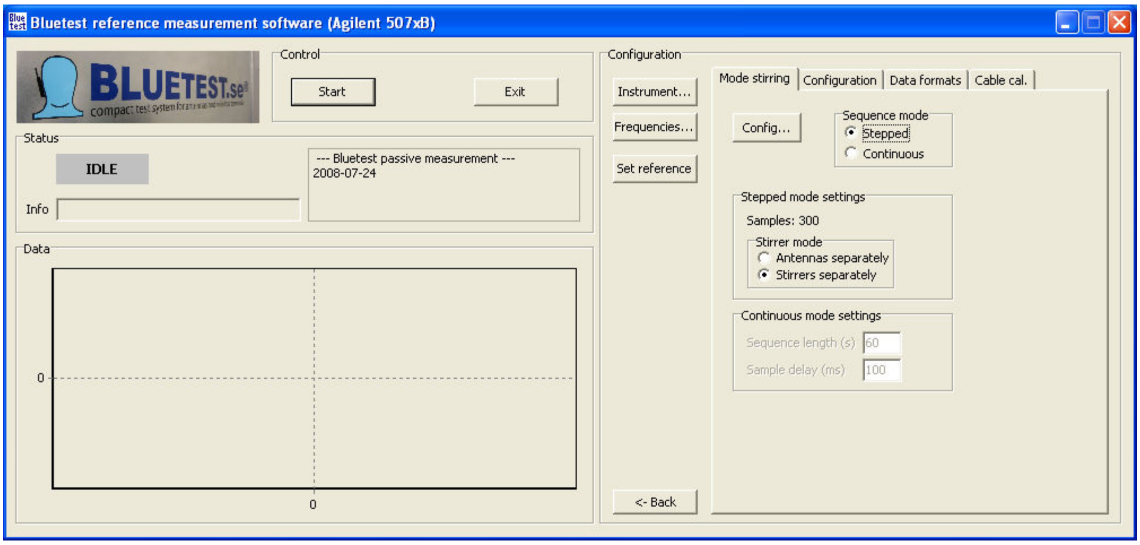

Figure 3.4: Bluetest software: reference measurements settings window.

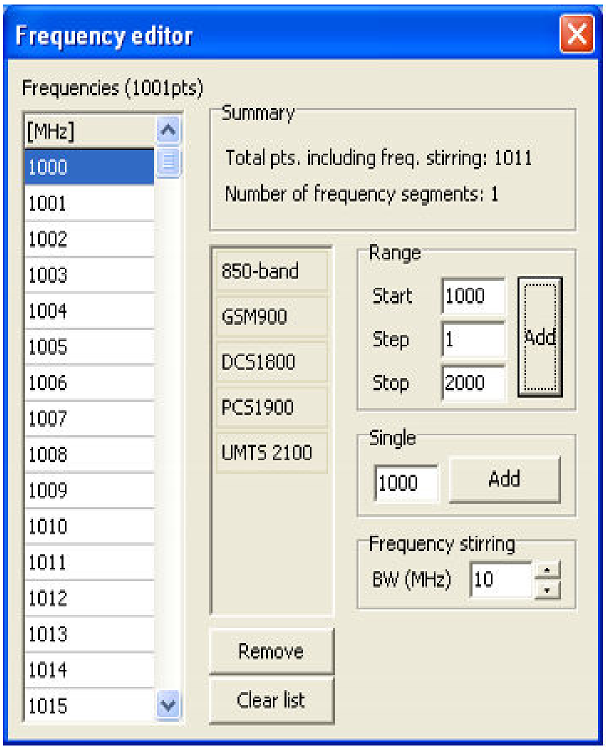

Figure 3.5: Bluetest software: frequency settings window.

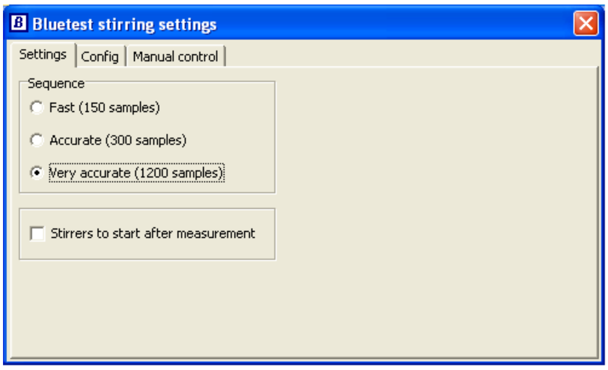

Figure 3.6: Bluetest software: stepped mode settings window.

3.5 Data Processing and Results

When a measurement is completed, the raw data are saved, processed and used to compute the chamber transfer function, which contains all the information about the transmissions inside the chamber, the stirrers' effectiveness and the accuracy of the measurements. The data processing is done by Matlab and here is shown a simple example of matlab code to estimate the chamber transfer function:

```
% Load data and path to get the measured raw data
meas_ref=LoadS('C:\Documents and Settings\Desktop\chalmers\measurement\
Bluetest_raw\20080225-1523-2970.s');

% Get S-parameter matrices from loaded structure:
s11 = cat(3,meas_ref.S{1}{1}{1},meas_ref.S{1}{1}{2},meas_ref.S{1}{1}{3});
s21 = cat(3,meas_ref.S{2}{1}{1},meas_ref.S{2}{1}{2},meas_ref.S{2}{1}{3});
s22 = cat(3,meas_ref.S{2}{2}{1},meas_ref.S{2}{2}{2},meas_ref.S{2}{2}{3});
freq = meas_ref.Frequencies;

% Complex average of s11 and s22 for the stirrer positions:
s11m = mean(s11,2);
s22m = mean(s22,2);

% Power avarage of s21 for the stirrer positions:
a21 = abs(s21);
p21 = a21.^2;
p21m = mean(p21,2);

% Correct for mismatch:
p21mc = p21m ./ ( (1-abs(s11m).^2) .* (1-abs(s22m).^2) );
p21mcs = squeeze(p21mc);

% Transfer Function averaged over the three wall antennas:
p21mcsp = mean(p21mcs,2);
```

After loading the raw data, we get the S-parameters S_{11}, S_{22} and S_{21} for each wall antenna. In one frequency point we have a raw of measured samples, one for each stirrer position. Thus, for the whole frequency range in which we want to measure, we obtain a matrix of measured samples. Then, we take the mean of S_{11}, S_{22} and $|S_{21}|^2$ over all the stirrer positions and we compute the transfer function for each wall antenna. Finally, we get the transfer function by taking the mean over the polarization stirrers. In Figures 3.7(a), (b) and (c), are shown the measured chamber transfer functions without frequency stirring and with a frequency stirring of 10 MHz and 20 MHz applied during the data processing, respectively. In all graphs are shown the transfer functions for each wall antenna (color curves) and their mean (black curve). For these measurements, the RC was loaded with a head phantom, measuring in a frequency range between 0.5 and 6 GHz. The color curves are displaced by 5dB relative to each other, for clarity; instead the lowest one is unchanged. As seen in (3.7), the transfer function is inversely proportional to the frequency. The accuracy of the estimated transfer function depends on its variance, since the measured power levels are random variables. Thus, in the Figures we can observe that the fading level (i.e., the variance of the average power) decreases as the frequency stirring increases, so that a better accuracy is attained when the frequency stirring is used.

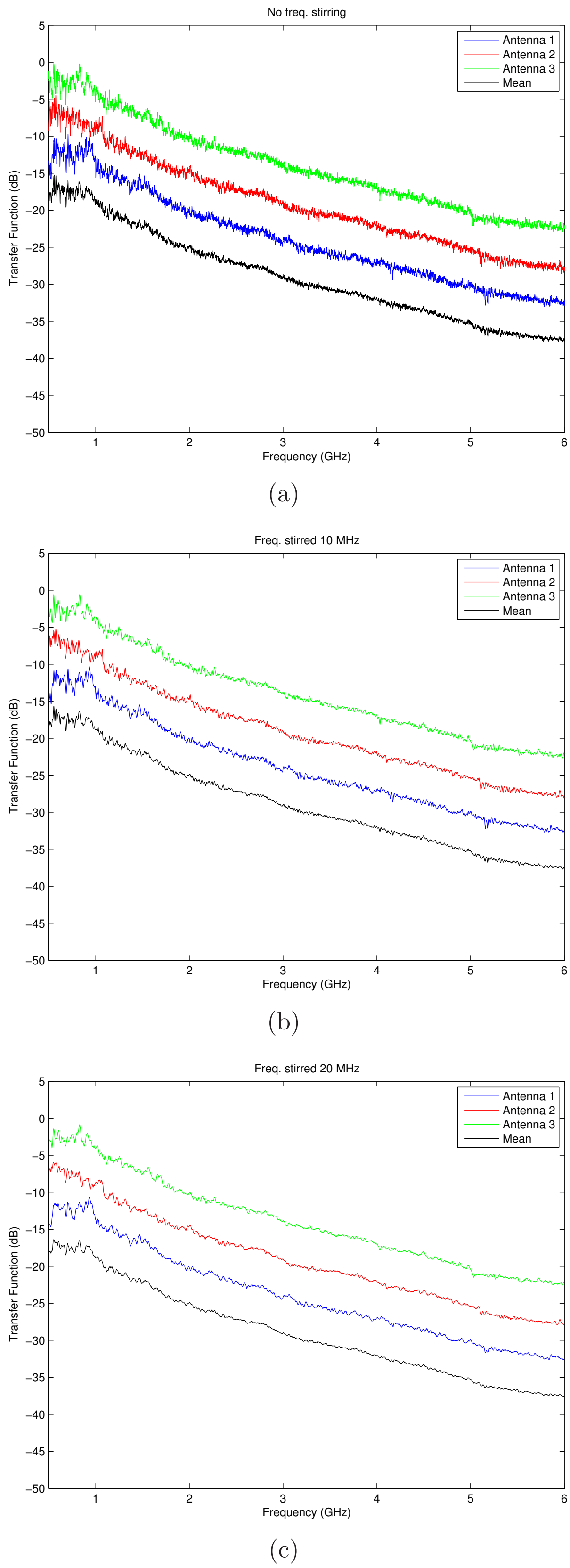

Figure 3.7: Measured chamber transfer function for each wall antenna (color curves) and their mean (black curve) without frequency stirring (a) and with frequency stirring of 10MHz (b) and 20MHz (c). The color curves are displaced by 5dB relative to each other, for clarity. The lowest is unchanged.

Chapter 4

Characterization of the Number of Independent Samples: New Theoretical Formula

4.1 Accuracy and Estimation of the Number of Independent Samples

In order to perform accurate measurements, the chamber transfer function needs to be proportional to the radiation efficiency independently of which antenna is used. This is only possible if the stirring mode can create enough independent samples. We define samples as the number of field distributions that are created and sampled. When a measurement is performed, a sequence of samples is obtained and the average of power transfer function levels is estimated. The measured samples are random variables with an average power transfer function that is normally distributed with a certain standard deviation σ. Thus, the relative accuracy by which we can estimate the power transfer function has a normalized standard deviation (STD) [23]

$$\sigma = \frac{1}{\sqrt{N_{\mathrm{ind}}}}, \tag{4.1}$$

where N_{ind} is the number of independent samples. The standard deviation in decibels is defined as

$$\sigma_{dB} = \pm\frac{1}{2}10\log\left(\frac{1+\sigma}{1-\sigma}\right) \tag{4.2}$$

(e.g., at least 100 independent samples are needed for an accuracy of ±0.5 dB). To obtain the efficiency of an antenna, we compare two power transfer functions with the same standard deviation (4.1). Since each power transfer function is estimated in an independent way (different measurements), the total variance is equal to the sum of the variances. Therefore, the total standard deviation by which we can estimate the accuracy is

$$\sigma = \frac{\sqrt{2}}{\sqrt{N_{\text{ind}}}}. \tag{4.3}$$

The number of independent samples is determined by how well the modes are stirred, since a large number of uncorrelated field distributions are needed in order to emulate an isotropic multipath environment with a uniform field inside the reverberation chamber. Thus, an important goal becomes to determine the importance of the different stirring methods in the calibration procedure. Moreover, a theoretical formula is needed to estimate the total number of independent samples such as we can compare it with the number of independent samples that can be obtained from the measurements. First, the number of independent samples is referred to the number of excited modes inside the cavity approximated as

$$N_{\text{excited}} = \frac{dN_{\text{modes}}}{df}\left(\Delta f + \Delta f_{\text{mech}} + B_{\text{FS}}\right), \tag{4.4}$$

where dN_{modes}/df is the mode density, i.e., the number of modes per MHz given by Weyl's Formula [24] [13] defined as

$$N_{\text{modes}} = \frac{8\pi}{3c^3}Vf^3. \tag{4.5}$$

Therefore, the number of excited modes in a reverberation chamber can be rewritten as

$$N_{\text{excited}} = \frac{8\pi}{c^3} V f^2 \left(\Delta f + \Delta f_{\text{mech}} + B_{\text{FS}}\right). \tag{4.6}$$

From (4.6), we can see that the number of excited modes increases when the stirring methods are enabled, since an additional bandwidth due to the mechanical (platform + plates) and frequency stirring will be added to the mode bandwidth. The number of excited modes is proportional to the chamber dimensions and by using the stirring methods we can virtually increase the chamber dimensions, thus exciting more modes. Furthermore, the number of excited modes gives an upper bound to the number of independent samples and it is defined [21] as

$$N_{\text{ind}} \leq 8\left[dN_{\text{modes}}/df\right]\left(\Delta f + \Delta f_{\text{mech}} + B_{\text{FS}}\right). \tag{4.7}$$

The factor eight considers that each mode is the sum of eight plane waves (see section 2.2.5). Moreover, by using the mechanical stirring, the antenna will also see different mode distributions ensuring eight times more independent samples than modes.

4.2 New Theoretical Formula for the Estimation of the Number of Independent Samples

The accuracy in reverberation chamber depends on the generation of a large number of independent samples. Some studies address ways for estimating the number of independent samples in a stirred chamber [10, 11, 13]. In this thesis, a new physical formula is developed for estimating the maximum number of independent samples in a reverberation chamber when different stirring methods are used. Moreover, the new formula can also be applied to other reverberation chambers with similar stirring methods. This study was performed using the Bluetest High Performance Reverberation Chamber at Chalmers University of Technology. Let us assume that the number of independent samples can be written as a product of different contributions when polarization, mechanical and frequency stirring are enabled. We can write that

$$N_{\text{ind}} = N_{\text{pol}} \cdot N_{\text{plates}} \cdot N_{\text{platf}} \cdot N_{\text{freq}}, \tag{4.8}$$

where $\mathrm{N_{pol}}$ is a constant with a value equal to 2 since it considers that both TE and TM modes can excite the receiving antenna separately. This contribution is only available after polarization stirring (i.e., after averaging the results over the three wall antennas). $\mathrm{N_{plates}}$ and $\mathrm{N_{platf}}$ are the number of independent samples obtained from the mechanical stirring, plates and platform, respectively. The last factor, $\mathrm{N_{freq}}$, is added in case the frequency stirring method is used.

4.2.1 New Theoretical formula for the Mechanical Stirring Case

The number of independent samples we can attain from mechanical stirring is referred to the number of mechanical positions considered during a measurement. We obtain a field sample for each platform and plates position. All measured samples are decorrelated only when all the platform and plates positions are independent. In order to determine when this happens, we need to define first the correlation length after which two consecutive platform or plate positions are independent. The spatial correlation function is defined as [25] [26]

$$\rho\left(\mathbf{r}_1, \mathbf{r}_2\right) = \frac{\sin\left(k\left|\mathbf{r}_1 - \mathbf{r}_2\right|\right)}{k\left|\mathbf{r}_1 - \mathbf{r}_2\right|}, \tag{4.9}$$

where $\mathrm{r_1}$ and $\mathrm{r_2}$ are two arbitrary locations inside the RC and k is the wave number. The correlation length $\mathrm{l_c}$ can be defined as the separation corresponding to the first zero in (4.9)

$$kl_c = \pi \Leftrightarrow l_c = \frac{\pi}{k} = \frac{\lambda}{2}. \tag{4.10}$$

Then, two samples are independent when the distance between two consecutive mechanical positions is greater than half wavelength. Let us consider first the platform stirring. We compare the distance between two consecutive platform positions with the correlation length. When the ratio between those two distances is bigger than one, the total number of platform positions gives the number of independent samples

$$N_{\text{platf}} = N_{\text{platf\_pos}}, \tag{4.11}$$

where $\mathrm{N}_{\text{platf\_pos}}$ is the total number of platform positions. When the ratio is smaller than one, the real number of independent samples is defined as

$$N_{\text{platf}} = \frac{l}{\lambda/2}, \tag{4.12}$$

where l is the distance between two consecutive platform positions multiplied by the total number of platform positions

$$l = 2r \sin\left(\frac{\theta}{2}\right) \cdot N_{\text{platf\_pos}}, \tag{4.13}$$

r is the distance between the receiving antenna and the centre of the platform and θ is the angle between two consecutive platform positions, equal to $\theta = 2\pi/N_{\text{platf\_pos}}$, as shown in Figure 4.1.

Thereby, we can join (4.11) and (4.12) and write the number of independent samples due to the platform stirring in a compact way as

$$N_{\text{platf}} = \min\left\{N_{\text{platf\_pos}}, \frac{l}{\lambda/2}\right\}. \tag{4.14}$$

A similar procedure is applied for estimating the number of independent samples due to the plates stirring. The reverberation chamber at Chalmers University contains two plates. The horizontal plate (plate1) moves vertically along the wall covering a distance of L = 140 cm. The vertical plate (plate2) moves horizontally and covers a total length of L = 155 cm along the other wall. Once again, we compare the distance between two consecutive plate positions

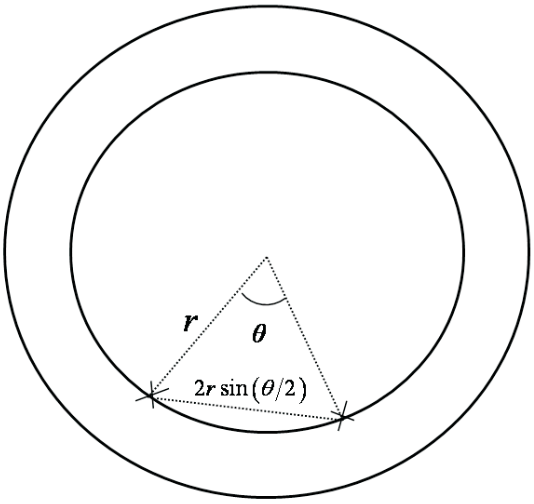

Figure 4.1: Illustration of two possible platform positions. The distance between two consecutive platform positions is computed by using the triangles principles.

with the correlation length. When the ratio is smaller than one, the number of independent plate positions is given by

$$N_{\text{plates}} = \frac{L}{\lambda/2}. \tag{4.15}$$

Instead, when the ratio of the distance between two consecutive plate positions and the correlation length is bigger than one, all plate positions are independent and

$$N_{\text{plates}} = N_{\text{plates\_pos}}. \tag{4.16}$$

The plates can move simultaneously or at different times. When they move simultaneously, we consider 10 plate positions for both plates. In this case, the number of independent samples is referred to the plate that covers the shortest length, i.e., plate1 with L = 140 cm. Then, the number of independent samples obtained from plates stirring is

$$N_{\text{plates}} = \min\left\{N_{\text{plates\_pos}}, \frac{L}{\lambda/2}\right\}. \tag{4.17}$$

4.2.2 New Theoretical formula for the Frequency Stirring Case

When the frequency stirring is used, the number of independent samples increases. Thus, an additional multiplicative factor, N_{freq}, is needed in (4.8). When processing the measured data at a certain frequency f, also the samples that are within the frequency stirring bandwidth B_{FS}, around f, are considered. Once again, we need to define a correlation length after which those samples are independent. The frequency deviation after which the correlation is lost corresponds to the average mode bandwidth Δf [27] [28]. Thus, in order to get decorrelated samples, we divide the frequency stirring bandwidth over the mode bandwidth. Since also the modes at the edges of the frequency stirring bandwidth will be excited, it is needed to add a $\Delta f/2$ contribution for each bandwidth side to the total B_{FS}, as shown in Figure 4.2. Then, we can write that the number of independent samples due to the frequency stirring is equal to

$$N_{\text{freq}} = \frac{B_{\text{FS}} + \Delta f}{\Delta f} = \frac{B_{\text{FS}}}{\Delta f} + 1. \tag{4.18}$$

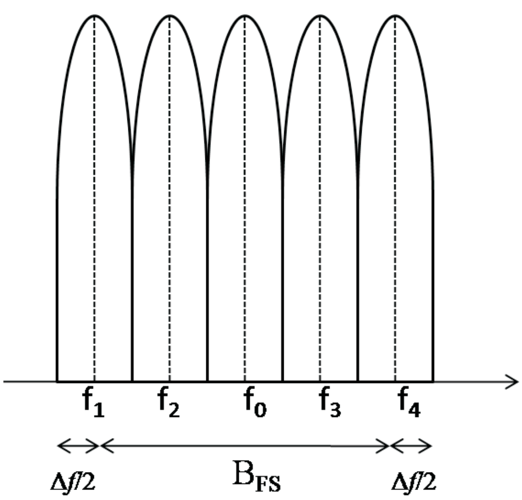

Figure 4.2: Subsection of the frequency stirring bandwidth into intervals of length equal to the average mode bandwidth Δf. The subsection also includes an additional $\Delta f/2$ for each side in order to include all the excited modes.

4.3 Number of Independent Samples Measured

Applying the new formulas, (4.8) can be rewritten as

$$N_{\text{ind\_theory}} = 2 \cdot \left(\min\left\{ N_{\text{platf\_pos}}, \frac{l}{\lambda/2} \right\} \right) \cdot \left(\min\left\{ N_{\text{plates\_pos}}, \frac{L}{\lambda/2} \right\} \right) \cdot \left(\frac{B_{\text{FS}} + \Delta f}{\Delta f} \right). \quad (4.19)$$

(4.19) considers the case in which both platform and plates are used, with the plates moving simultaneously and considering the same number of plates positions. However, we can use the two plates at different times by modifying the new formula with an additional factor due to the second plate. In order to evaluate the accuracy of the calibration procedure, we will perform it twice and compare the results of the power transfer function. First, we place the disk-cone antenna in the chamber and we measure the power transfer level. Then, we perform another measurement with the same antenna located in a different orientation and height inside the chamber, obtaining a different power transfer function level. Although we use the same antenna for both cases, the two measurements are independent since they are done using different orientations, positions and height of the antenna inside the chamber. Thus, we can consider the first case as the reference case and the second as the test case. The deviations between the two power levels provide an estimate of the measurements accuracy. We compute the error as the relative difference between the average power levels of the two cases [29]

$$e(f) = \frac{P_{\text{AUT}}(f) - P_{\text{ref}}(f)}{P_{\text{ref}}(f)}. \quad (4.20)$$

Then, the standard deviation of the relative error is

$$\sigma = STD\left[e(f)\right] = \sqrt{\frac{1}{N_{\text{fpoint}} - 1} \sum_{i=1}^{N_{\text{fpoint}}} \left\{e(f_i)\right\}^2}, \quad (4.21)$$

where N_{fpoint}, is the number of frequency points, i.e., the whole frequency interval in which we want to perform the measurement. The errors are uncorrelated at different frequencies ensuring that we are evaluating the standard deviation in the correct way. Hence, the number of independent samples measured can be easily attained using (4.3) as

$$N_{\text{ind\_measured}} = \frac{2}{\sigma^2}, \tag{4.22}$$

where σ is the standard deviation of the averaged power levels found in (4.21).

Chapter 5

Measurements and Results

5.1 Measurements Setup

All the considerations done in the previous chapter need to be validated by measurements. In addition, in order to determine the importance of the stirring methods in the calibration procedure, several measurements are needed. Thus, we first measured the disk cone antenna in the horizontal position, located at a height of 29 cm from the platform, and we used it as reference case. Then, the disk cone antenna in the vertical position, height 55 cm from the platform, was measured as test case. Using the same antenna does not give ambiguity in the results, since each measurement is done with different orientation and height, making independent measurements. The measurements were performed in a wide frequency range from 0.5 to 6 GHz, with step of 1 MHz, dividing the whole band in the following sub-bands: 0.5-1 GHz, 1-2 GHz, 2-3 GHz, 3-4 GHz, 4-5 GHz and 5-6 GHz. Afterwards, the results for the number of independent samples were compared from band to band. As alternative, we could measure many more times with different positions and orientations in order to observe the frequency variation of the number of independent samples within each sub-band. However, this would require many more measurements and time. The same measurements were done for both empty chamber and chamber loaded with a head phantom. The head phantom is filled with liquid that has electrical properties comparable to those of human brain tissue, as specified by the European Standard EN 5061. By modifying the control software of the chamber, we could measure using different stirring configurations and change the number of plates and platform positions. All the measurements were done using the stepped mode (see section 3.4) and performed with three different steps:

- Both plates and platform are enabled
- Only plates are enabled
- Only platform is enabled

During the data processing frequency stirring bandwidths of 1 MHz, 2 MHz, 4 MHz, 8 MHz, 16 MHz, 32 MHz, 64 MHz and 100 MHz were used. In addition, for each band the measured data are plotted considering several mechanical positions and a comparison between the number of independent samples measured and theoretical is presented.

5.2 Platform and Plates Stirring Case

In this case all the stirring methods are applied. By modifying the control software we can set the total number of platform positions to 40. The number of plates positions for each platform position is fixed to 10 and in this case they move simultaneously. For each platform position the control software stores $3 \times 10 = 30$ transmission samples, since the three wall antennas excite together the chamber. Hence, the total number of samples obtained is $40 \times 30 = 1200$, i.e., 400 samples for each wall antenna. By applying (4.19) and (4.22) we can estimate the theoretical and measured number of independent samples achieved in this case. Figures 5.1 and 5.2 show the behavior in logarithmic scale of $\mathrm{N_{ind\_measured}}$ (continuous lines) and $\mathrm{N_{ind\_theory}}$ (dashed lines) for the empty chamber and the loaded chamber case, respectively. All the results are shown without frequency stirring ($\mathrm{B_{FS}}$ = 1 MHz) and with frequency stirring applied. In order to see the differences when the number of samples is varying, the measured data are processed considering 5, 10, 20 and 40 platform positions. Thus, the total number of samples for each wall antenna is 50, 100, 200 and 400, as shown in the Figures (colored curves). First of all, we can notice a really good agreement between theory and measurements, which shows that the new formula is a good estimator of the number of independent samples especially at the higher frequency bands. However, in the lower frequencies the theory seems not to match well with the measurements (above all in the loaded chamber case). Some investigations in this direction were done, showing that a residual direct coupling between the transmitting and the receiving antenna is present at low frequencies (see next section). An unusual behavior appears in the range between 2 GHz and 3 GHz, in which $\mathrm{N}_{\mathrm{ind\_measured}}$ seems not to increase at the higher frequency stirring bandwidths. The reason can be attributed to some cables inside the chamber that caused problems also in previous measurements and in the same range. Figures show the number of independent samples increase when the frequency increases. It is plausible since at high frequency the chamber size is larger compared to the wavelength and more modes are excited. We also notice that in the loading case the number of independent samples obtained when the frequency stirring increases is lower compared to the one attained in the empty chamber case. It is reasonable since when the mode bandwidth increases (loaded case), less samples within the frequency stirring bandwidth become decorrelated. As shown in the first subplots (0.5-1 GHz), the number of independent samples does not increase until the frequency stirring become very high. The cause can be addressed to the poor mode density below 1GHz, range where maybe the frequency stirring is not effective enough to cope with the few modes at least until a very large B_{FS} is used.

5.2.1 Residual Direct Coupling

In Figures 5.3 and 5.4 all the previous results are plotted for empty and loaded case considering the measured standard deviation found in (4.21) (continuous lines) and the theoretical one obtained by substituting (4.19) in (4.3) (dashed lines). As explained previously, theory and measurements do not agree at the lower frequencies as well as they do at high frequencies above all in the phantom case. This section will show that the reason of this mismatch is due to a not negligible residual direct coupling between the receiving and the transmitting antenna at the lower frequencies. In order to figure out this residual term, some observations about the average transfer function are needed. In a non-well stirred

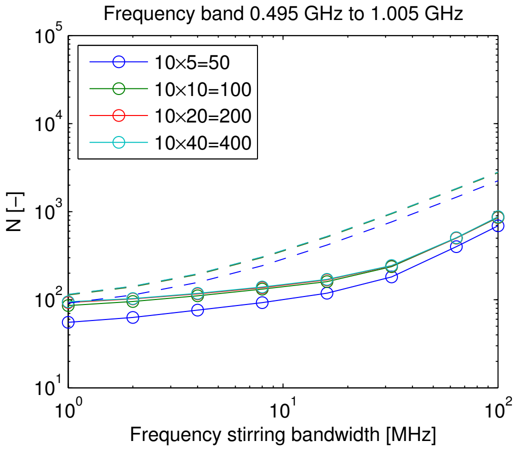

(a)

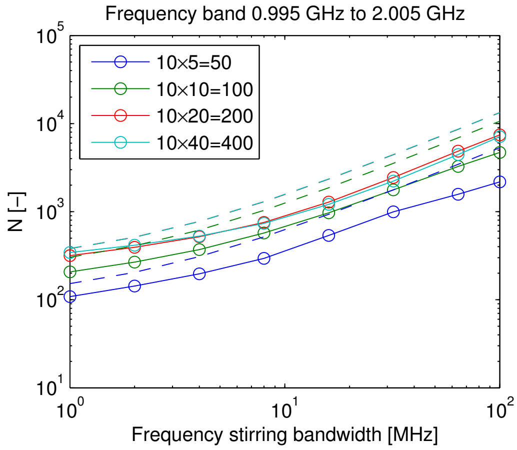

(b)

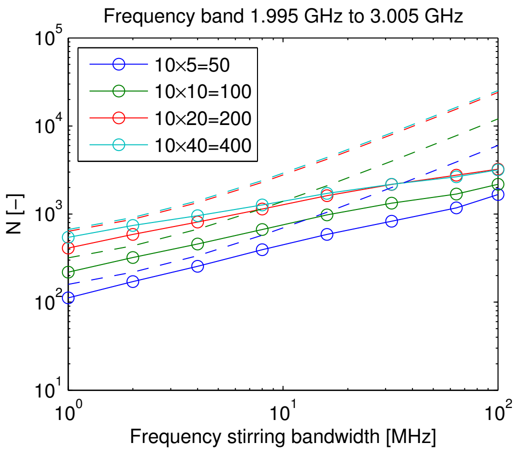

(c)

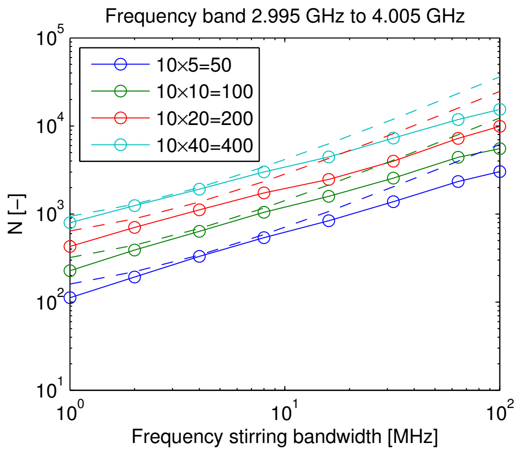

(d)

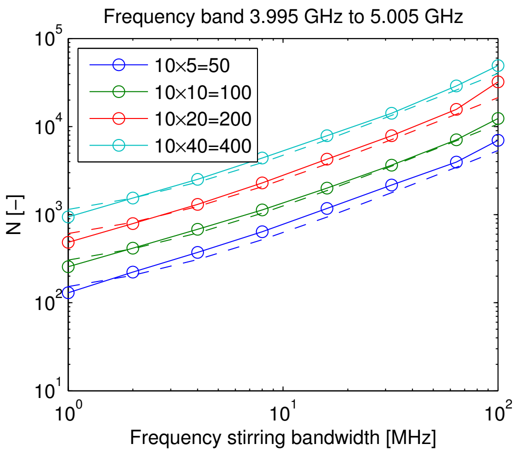

(e)

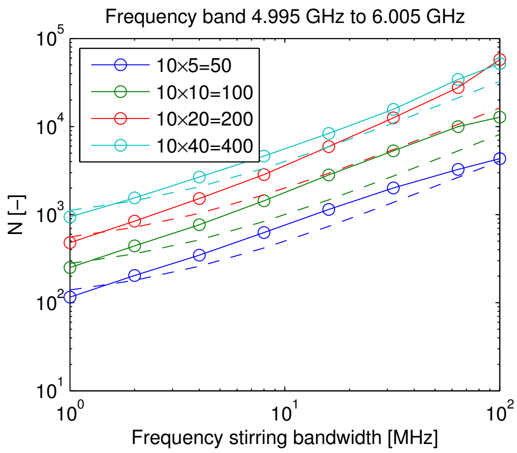

(f)

Figure 5.1: Number of independent samples obtained from measurements (continuous lines) and theory (dashed lines). The data are processed in logarithmic scale for each sub-band considering 5, 10, 20 and 40 platform positions and using a frequency stirring bandwidth going from 1 MHz to 100 MHz. Empty chamber case.

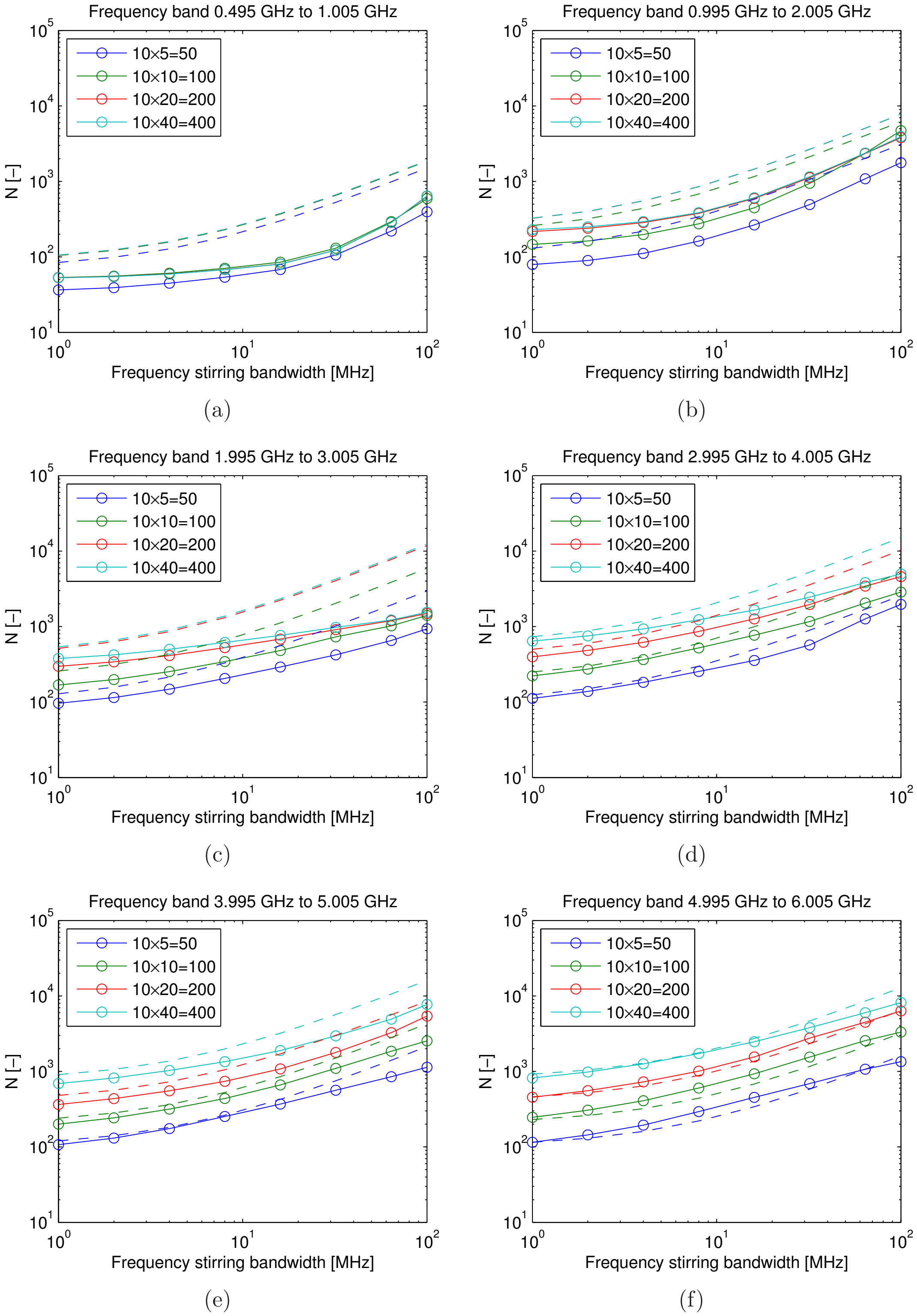

Figure 5.2: Number of independent samples obtained from measurements (continuous lines) and theory (dashed lines). The data are processed in logarithmic scale for each sub-band considering 5, 10, 20 and 40 platform positions and using a frequency stirring bandwidth going from 1 MHz to 100 MHz. Head phantom case.

RC, the received power can be written as the sum of a stirred and unstirred component as

$$P_r = P_{\text{stirred}} + P_{\text{unstirred}}, \tag{5.1}$$

where P_{stirred} is the power due to the incoherent part of the field and $P_{\text{unstirred}}$ is the power due to the direct coupling between the AUT and the excitation antenna.

Thus, from (5.1) the power transfer function can be written as

$$\frac{P_r}{P_t} = \frac{P_{\text{stirred}} + P_{\text{unstirred}}}{P_t} = \frac{P_{\text{stirred}}}{P_t} \cdot \left(1 + \frac{P_{\text{unstirred}}}{P_{\text{stirred}}}\right). \tag{5.2}$$

The quantity P_{stirred}/P_t is the transfer function of a well stirred chamber given by Hill's Formula (see section 3.2.2) and defined as

$$\frac{P_{\text{stirred}}}{P_t} = \frac{c^3}{16\pi^2 V f^2 \Delta f}, \tag{5.3}$$

in which we assumed the efficiencies of the receiving and transmitting antenna are equal to one. The ratio $P_{\text{unstirred}}/P_{\text{stirred}}$ represents the Rician K-factor defined as [4]

$$\frac{P_{\text{unstirred}}}{P_{\text{stirred}}} = K = \frac{3}{2}\frac{V}{\lambda Q}\frac{D}{r^2}, \tag{5.4}$$

where V is the chamber volume, λ is the wavelength, Q is the chamber quality factor, r is the distance between the AUT and the transmitting antenna and D is the pattern of the receiving antenna. Assuming that D = 1, we can substitute (5.3) and (5.4) in (5.2) and after some simple computations, we can write that

$$\frac{P_r}{P_t} = \frac{P_{\text{stirred}}}{P_t} \cdot (1 + K) = \frac{P_{\text{stirred}}}{P_t} + \frac{3}{2}\left(\frac{\lambda}{4\pi r}\right)^2, \tag{5.5}$$

where P_{stirred}/P_t is the power transfer function of a well-stirred chamber that we

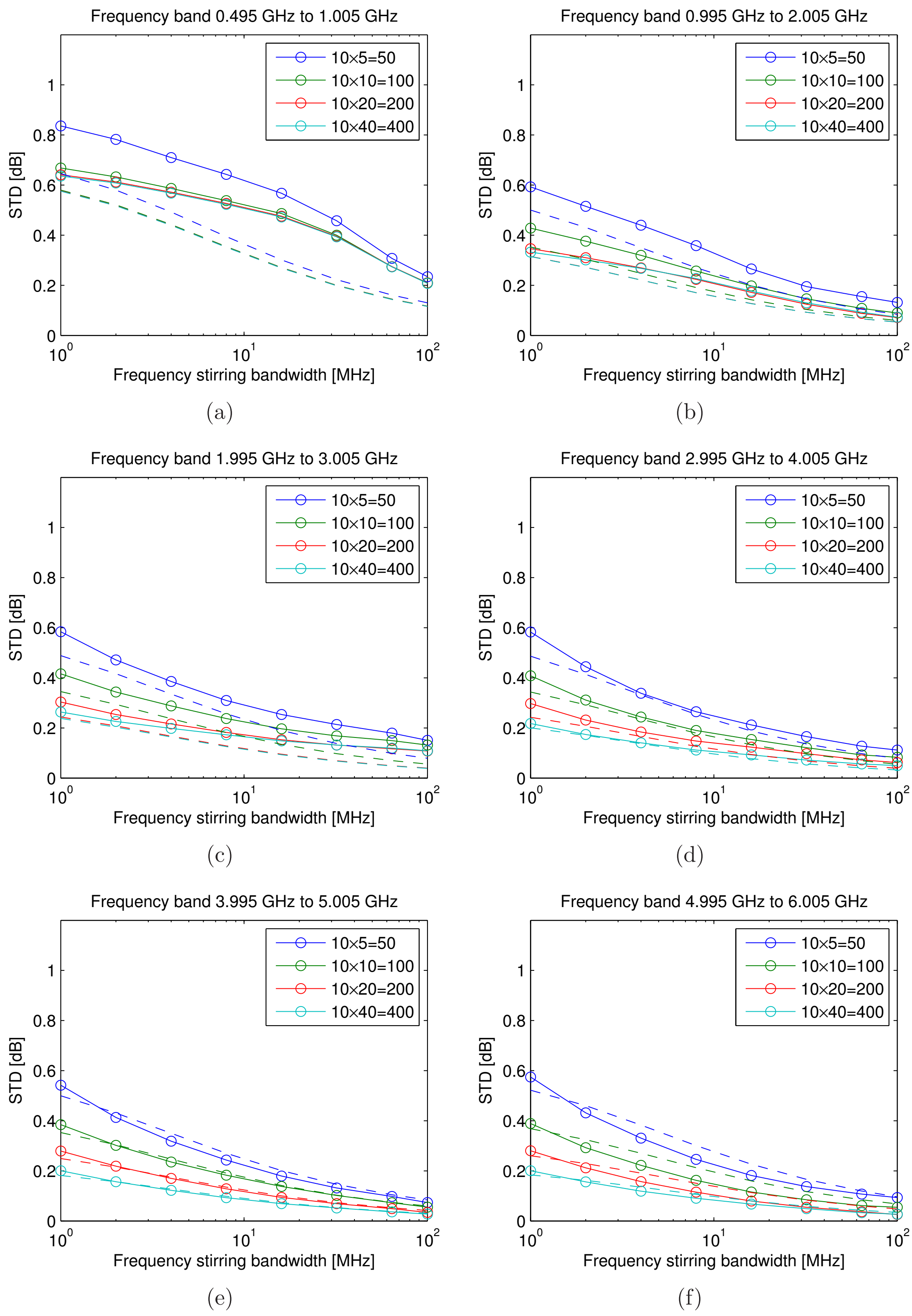

Figure 5.3: STD in dB value obtained from measurements (continuous lines) and theory (dashed lines). The data are processed for each sub-band considering 5, 10, 20 and 40 platform positions and using a frequency stirring bandwidth going from 1 MHz to 100 MHz. Empty chamber case.

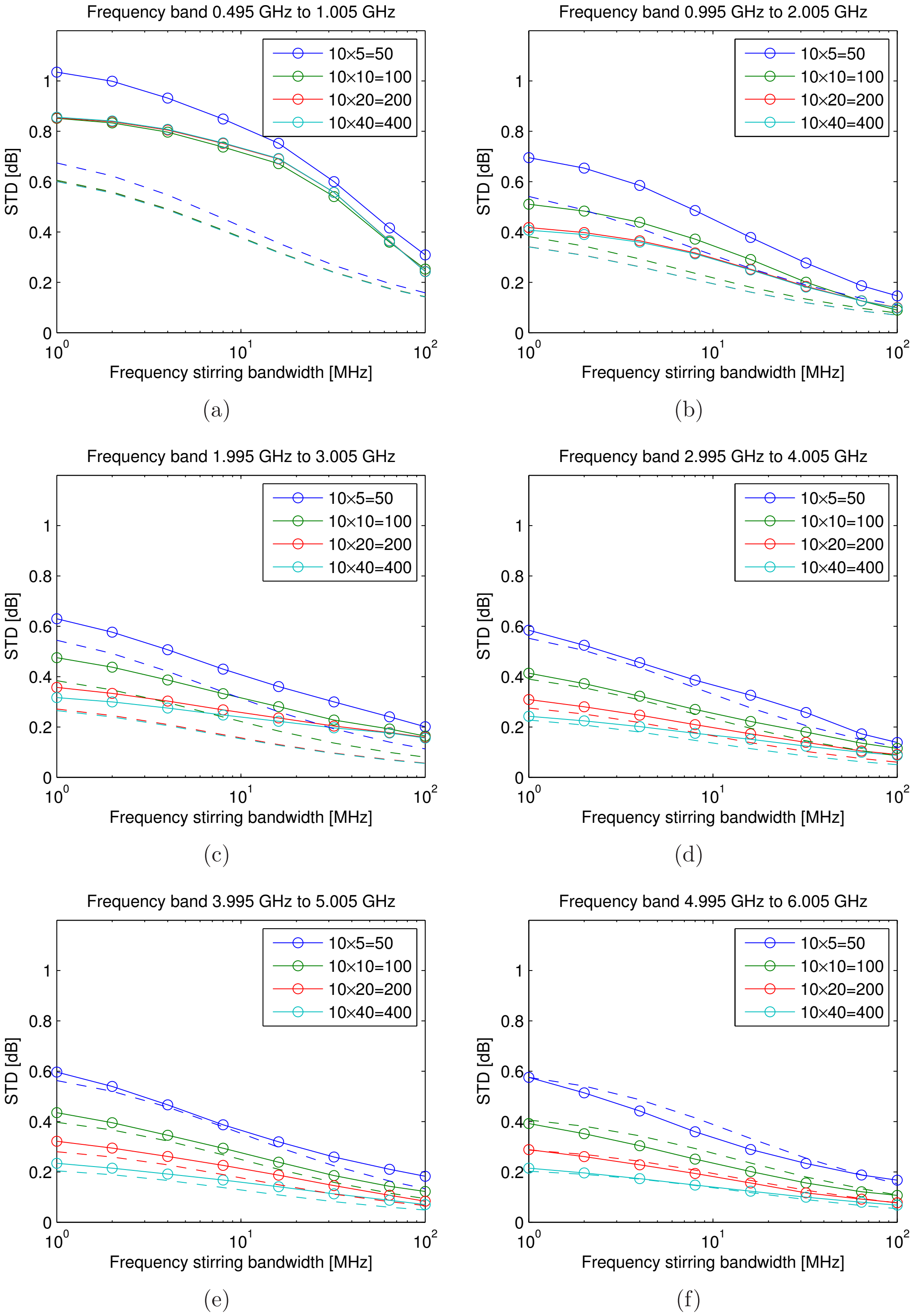

Figure 5.4: STD in dB value obtained from measurements (continuous lines) and theory (dashed lines). The data are processed for each sub-band considering 5, 10, 20 and 40 platform positions and using a frequency stirring bandwidth going from 1 MHz to 100 MHz. Head phantom case.

call $\mathrm{P_s}$. The second term of (5.5) represents the power transfer function due to a residual unstirred component, i.e., a residual direct coupling between the receiving and the transmitting antennas that we call $\mathrm{P_{dc}}$. Then, we can write that the chamber transfer function in a non-well stirred RC is

$$\frac{P_r}{P_t} = P_\mathrm{s} + P_\mathrm{dc}, \tag{5.6}$$

where

$$P_\mathrm{dc} = \frac{3}{2}\left(\frac{\lambda}{4\pi r}\right)^2. \tag{5.7}$$

From (5.7) we can see that the residual direct coupling is proportional to the ratio λ/r. At high frequencies, this ratio is really small and the contribution due to the direct coupling can be negligible compared to the power of the stirred component. This does not happen in the lower frequencies where $\mathrm{P_{dc}}$ is comparable with $\mathrm{P_s}$ and can not be neglected. Moreover, when the chamber is loaded with lossy object, $\mathrm{P_{dc}}$ is even greater compared to $\mathrm{P_s}$, since the mode bandwidth increases when extra losses are presents. Thus, a better accuracy can be achieved in the lower frequencies if the term due to residual direct coupling is removed. Let us consider the variance of the measured values as

$$\sigma_\mathrm{m}^2 = \mathrm{var}\left(\frac{P_\mathrm{AUT} - P_\mathrm{ref}}{P_\mathrm{ref}}\right) = \mathrm{var}\left(\frac{P_\mathrm{s} - P_\mathrm{ref}}{P_\mathrm{ref}} + \frac{P_\mathrm{dc}}{P_\mathrm{ref}}\right). \tag{5.8}$$

Since the two ratios inside the round brackets are independent, the variance of the sum is equal to the sum of the variances. Hence, (5.8) can be written as

$$\sigma_\mathrm{m}^2 = \sigma_\mathrm{t}^2 + \sigma_\mathrm{res}^2, \tag{5.9}$$

where σ_t^2 is the variance of a well stirred RC and from the theory we already know that it is equal to

$$\sigma_\mathrm{t}^2 = \frac{2}{N_\mathrm{ind}}. \tag{5.10}$$

σ_{res}^2 is the variance due to the residual direct coupling. Substituting (5.7) in (5.8), we can determine σ_{res}^2 by the approximated formula

$$\sigma_{\text{res}}^2 \simeq \mathrm{C} \cdot \mathrm{var}\left(\frac{\lambda^2}{\mathrm{P}_{\text{ref}}}\right). \tag{5.11}$$

where C is a constant. From (5.9) it can be seen that when the theoretical value is equal to the measured one, i.e., when the power transfer function of the AUT is equal to the power of a well-stirred chamber (i.e., $\mathrm{P_s}$), $\sigma_{\text{res}}^2 = 0$. Otherwise, the measured variance is equal to the sum of the theoretical and the residual ones. From (5.11) we can obtain the residual standard deviation and we can see that it is proportional to the wavelength. Thus, by removing σ_{res} from the measured STD in (4.21) we attain a better accuracy in the lower frequencies. In Figures 5.5 and 5.6 are shown the results for the standard deviation (for the empty and loaded chamber case) when σ_{res} is removed. The results show better agreement between theory and measurements in the lower frequency ranges. No changes are present at the high frequency ranges compared to case in which the residual STD is present, since the direct coupling is negligible compared to the power of the stirred component.

5.3 Plates Stirring Case

By modifying the control software of the chamber, the platform can be stopped and the measurements are performed letting work only the plates. In this case the plates are moving in different times and for each plate2 position the total number of the plate1 positions is 20. Thus, the control software stores $20 \times 3 = 60$ samples for each plate2 position. Since the number of the plate2 positions used is 20, the total number of samples collected is $20 \times 60 = 1200$, i.e., 400 samples for each wall antenna. In Figures 5.7 and 5.8 are shown the results for the number of independent samples attained from the new theory and the measurements for empty chamber and chamber loaded with head phantom, respectively. The measured data are processed considering several plate1 positions, i.e., for 3, 5, 10 and 20 plate1 positions. As can be seen, the number of independent samples

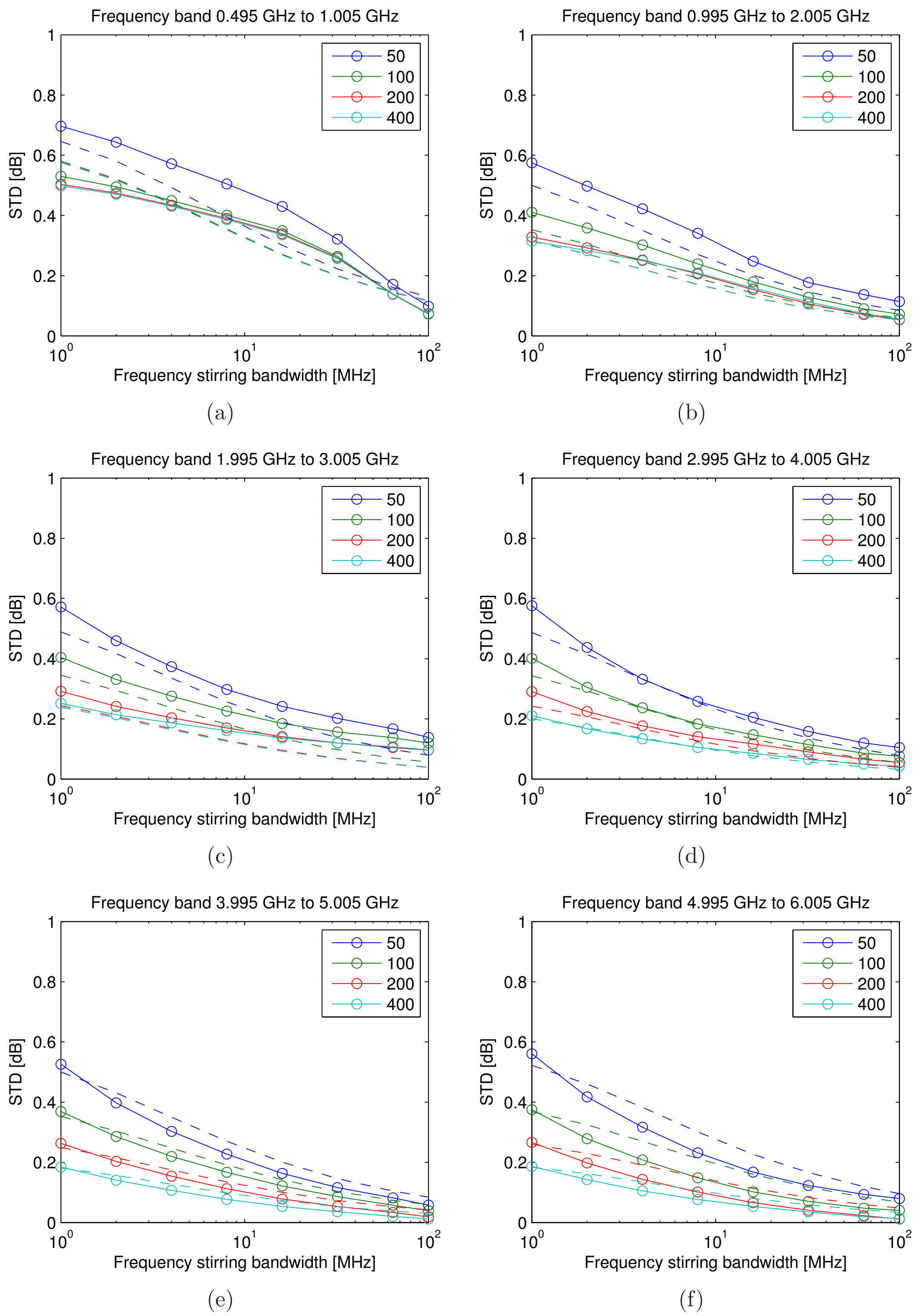

Figure 5.5: STD without residual direct coupling in dB value obtained from measurements (continuous lines) and theory (dashed lines). The data are processed for each sub-band considering 5, 10, 20 and 40 platform positions and using a frequency stirring bandwidth going from 1 MHz to 100 MHz. Empty chamber case.

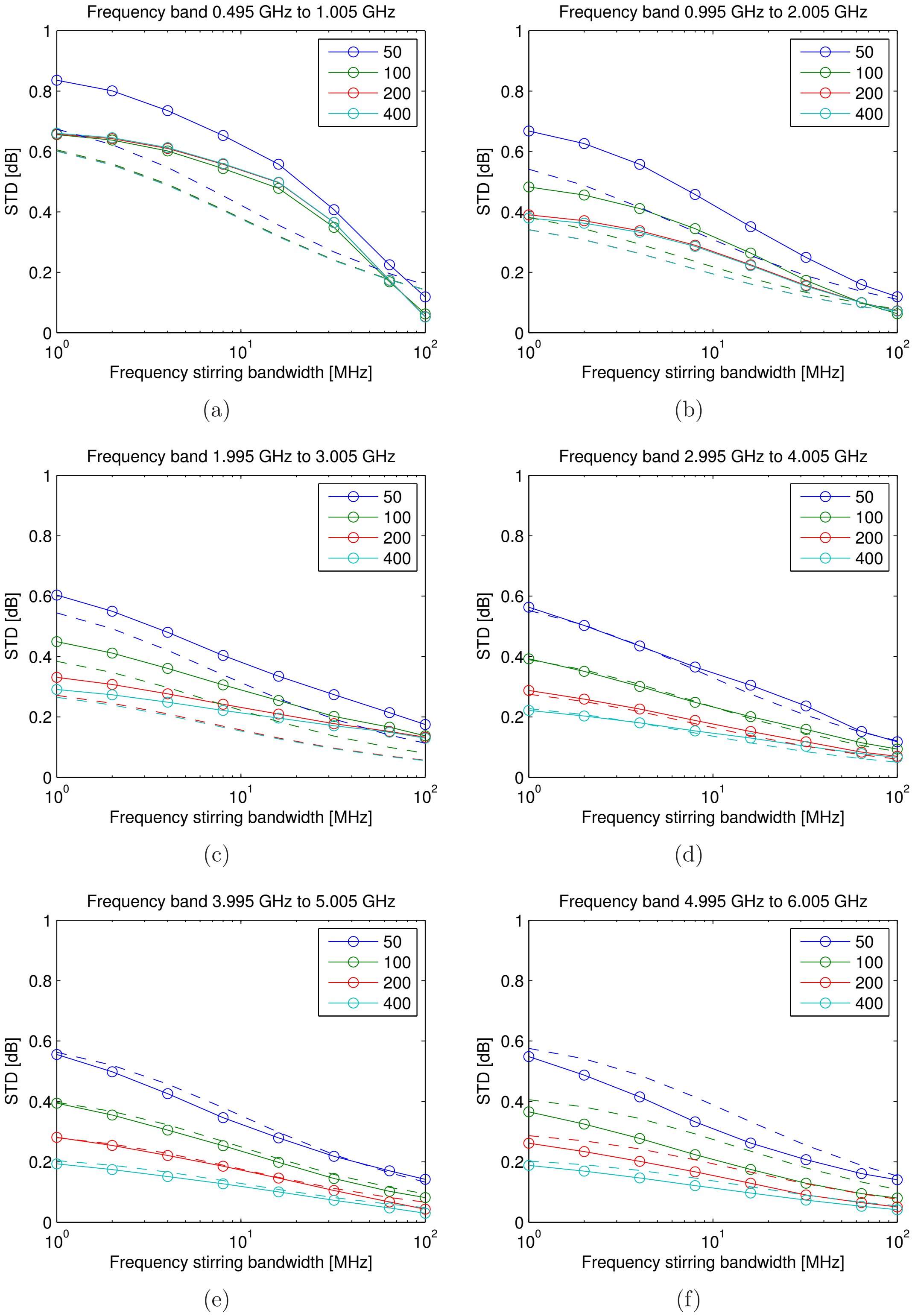

Figure 5.6: STD without residual direct coupling in dB value obtained from measurements (continuous lines) and theory (dashed lines). The data are processed for each sub-band considering 5, 10, 20 and 40 platform positions and using a frequency stirring bandwidth going from 1 MHz to 100 MHz. Head phantom case.

measured is small compared to the one we can attain from the theory. The mismatch is even bigger in the lower frequency ranges, in which $N_{ind\_measured}$ does not reach the threshold of 10^2 when frequency stirring is not used and the disagreement is stronger in the head phantom case. The reason is due the strong direct coupling between the AUT and the wall antennas. In this case the platform is not working, thus the AUT is stopped and the direct signals between it and the wall antennas can not be removed.

5.3.1 Complex S_{21} Stirring

A new solution needs to be found to improve the measurements accuracy when the platform stirring is not used. The direct coupling between the receiving antenna and the three wall antennas is the reason of the accuracy reduction. A simple method, called complex S_{21} stirring is presented in order to remove the direct coupling for this case. It consists in removing the mean over all the stirrer positions from the complex S_{21} during the data processing. First the mean of S_{21} over all the stirrer positions is computed for each wall antenna. Then, each mean is removed from the complex S_{21} and the power transfer function is calculated. The results for the number of independent samples when complex S_{21} stirring is applied are shown in Figures 5.9 and 5.10 for the empty and loading case. The theory has not changed, only the measured data are processed in a different way. An improvement can be noticed in all frequency ranges (in both empty and loaded chamber cases) compared to the cases in which the complex S_{21} stirring is not used. Theory and measurements almost agree as in the case in which the platform is also enabled. Although it could be difficult to apply the complex S_{21} stirring in the active measurements, those results aware us that the platform works well, since with its contribution we can remove the direct coupling as well as we can do by complex S_{21} stirring.

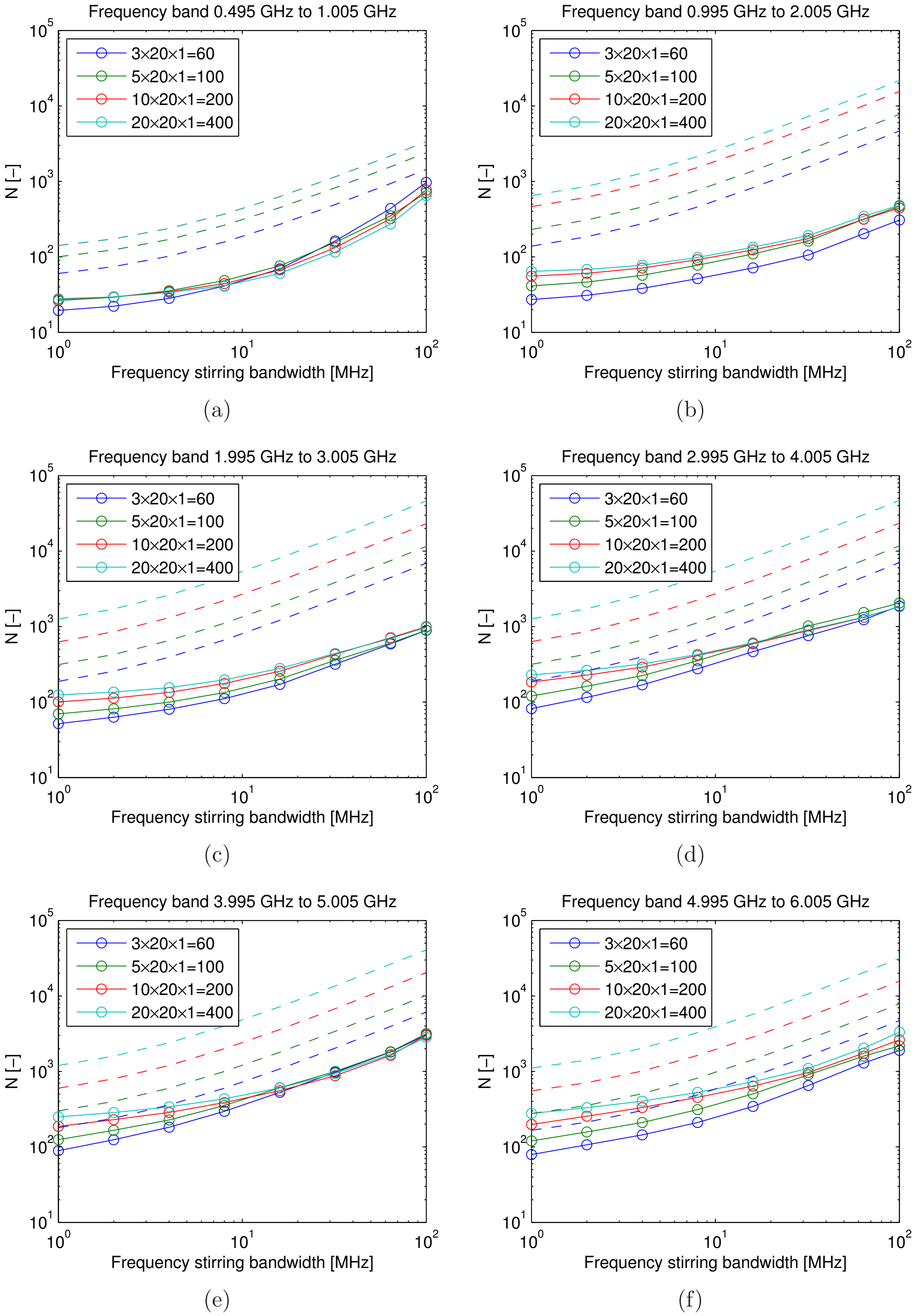

Figure 5.7: Number of independent samples obtained from measurements (continuous lines) and theory (dashed lines) when platform stirring is stopped. The data are processed in logarithmic scale for each sub-band considering 3, 5, 10 and 20 plate positions and using a frequency stirring bandwidth going from 1 MHz to 100 MHz. Empty chamber case.

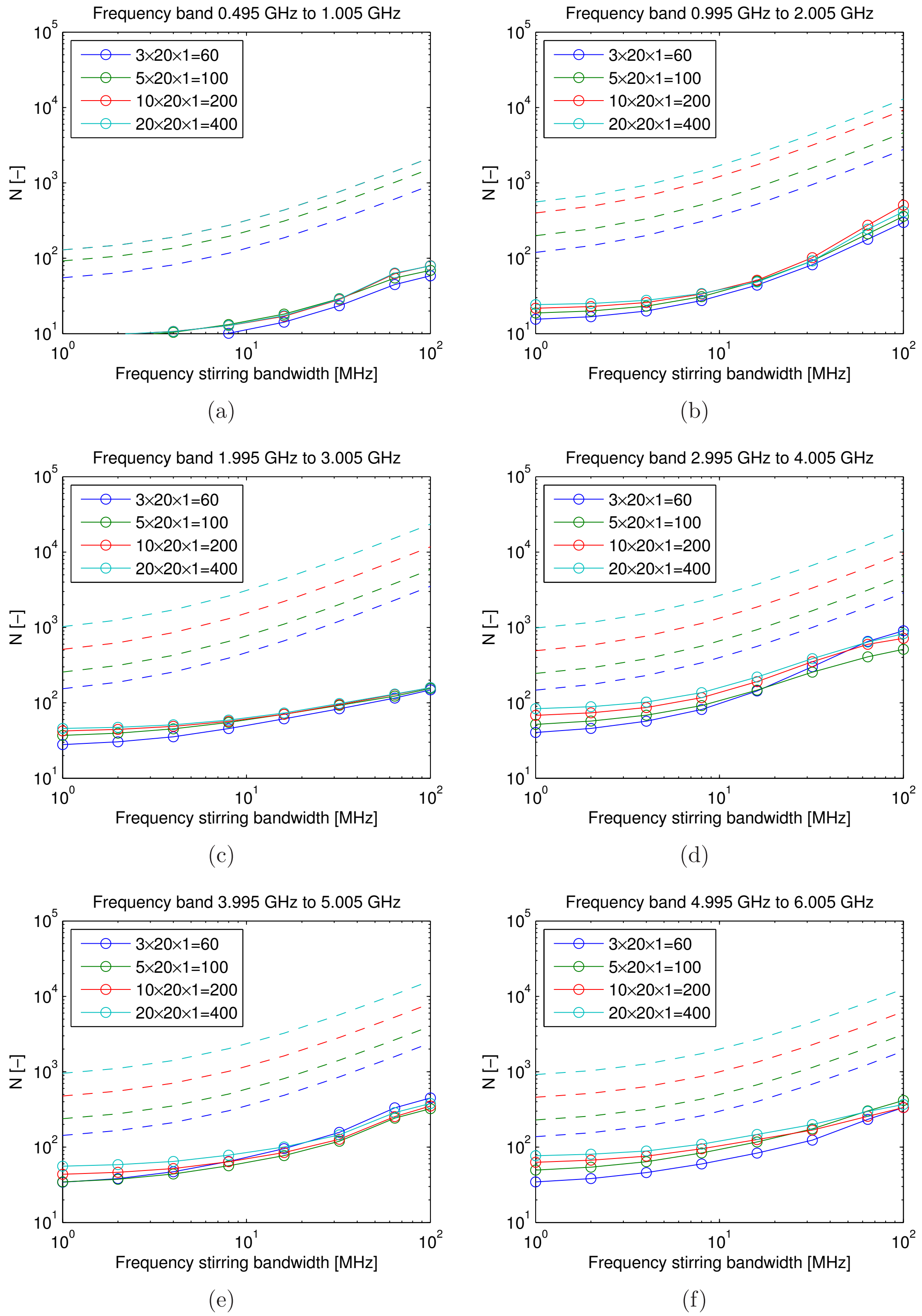

Figure 5.8: Number of independent samples obtained from measurements (continuous lines) and theory (dashed lines) when platform stirring is stopped. The data are processed in logarithmic scale for each sub-band considering 3, 5, 10 and 20 plate positions and using a frequency stirring bandwidth going from 1 MHz to 100 MHz. Head phantom case.

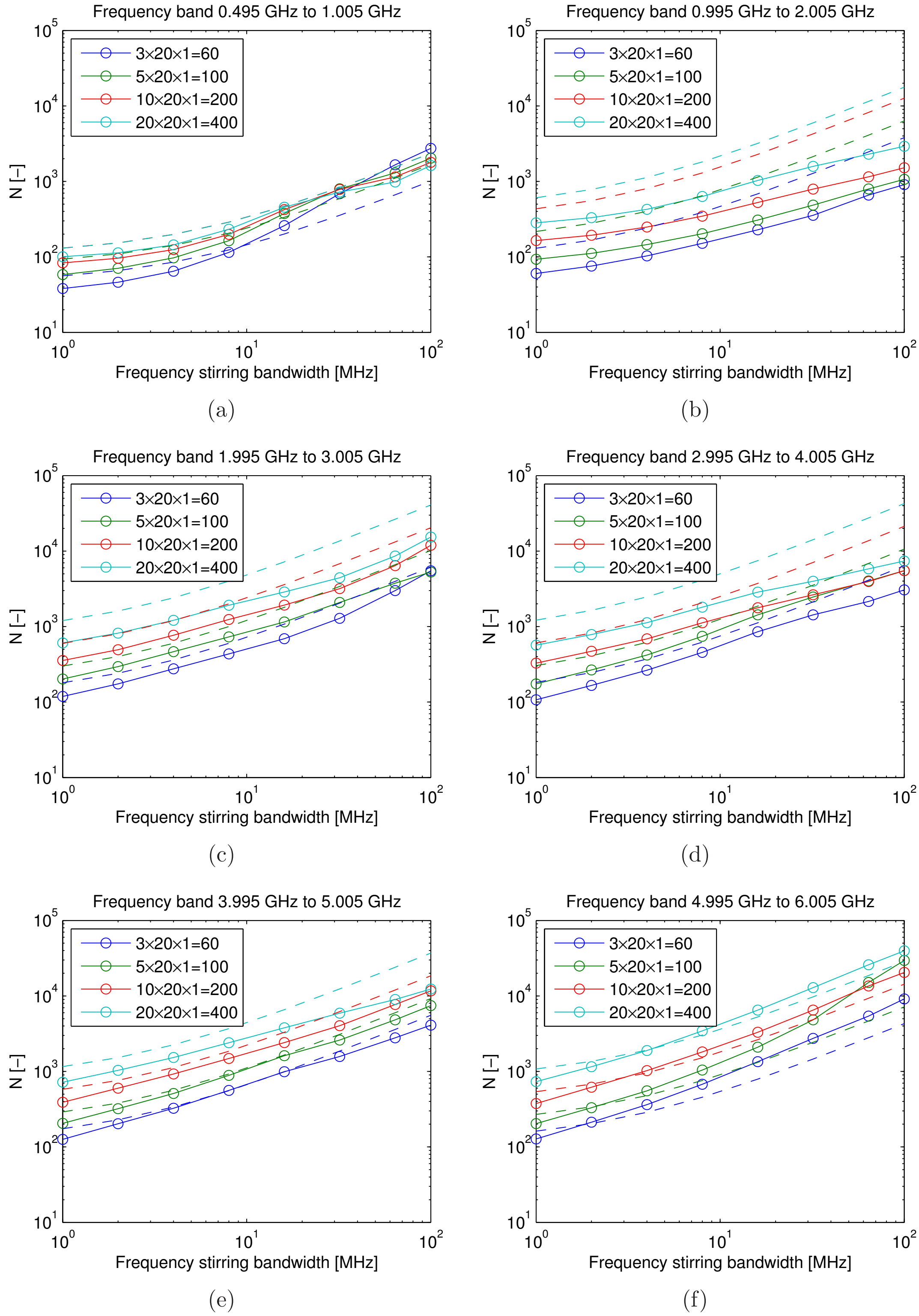

Figure 5.9: Number of independent samples obtained from measurements (continuous lines) and theory (dashed lines) when the complex S_{21} stirring is applied. The data are processed in logarithmic scale for each sub-band considering 3, 5, 10 and 20 plate positions and using a frequency stirring bandwidth going from 1 MHz to 100 MHz. Empty chamber case.

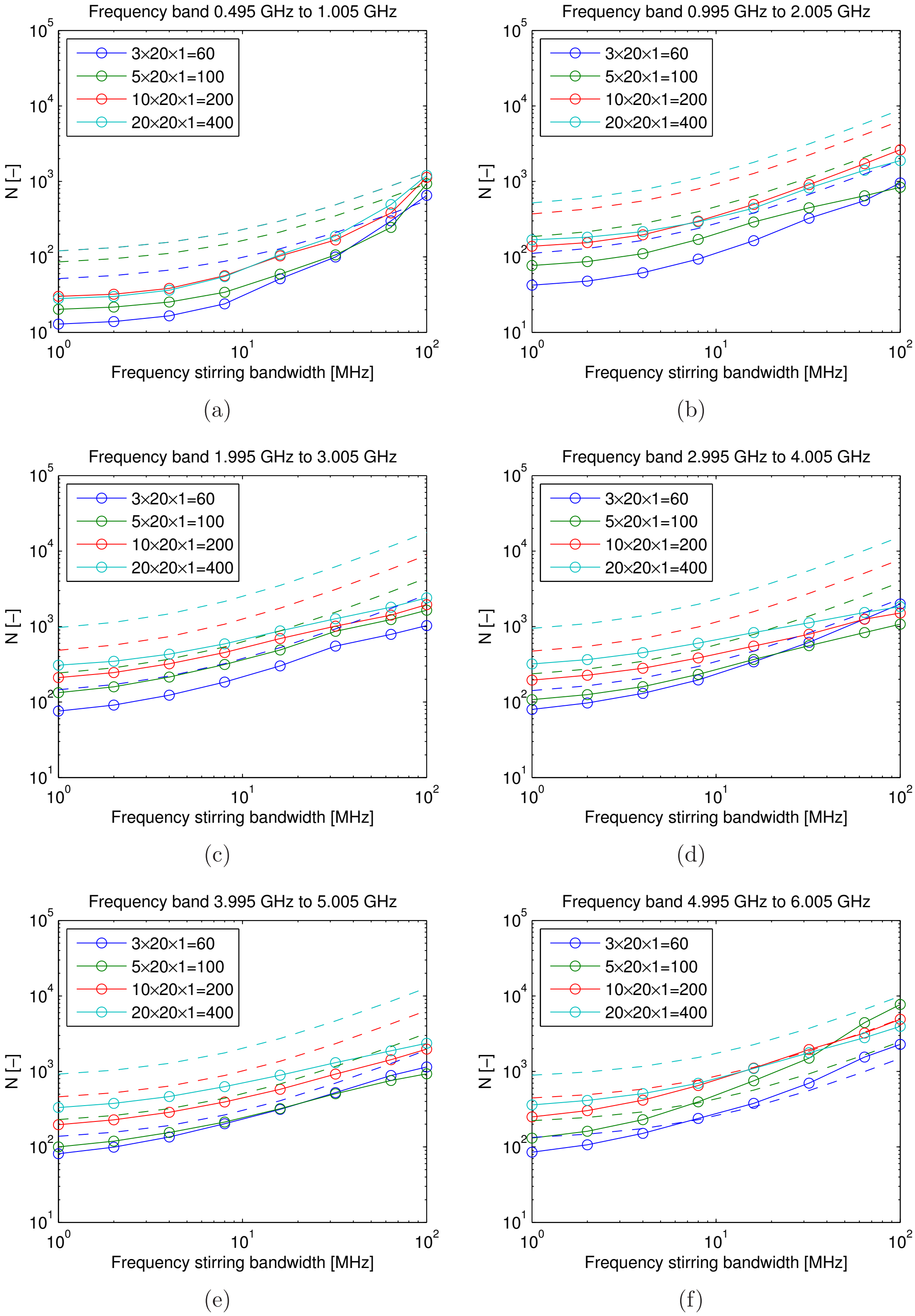

Figure 5.10: Number of independent samples obtained from measurements (continuous lines) and theory (dashed lines) when the complex S_{21} stirring is applied. The data are processed in logarithmic scale for each sub-band considering 3, 5, 10 and 20 plate positions and using a frequency stirring bandwidth going from 1 MHz to 100 MHz. Head phantom case.

5.4 Platform Stirring Case

In this case only the platform is enabled. By modifying the control software we can stop the plates and choose the total number of platform position we want to use during the measurements. All the setup is the same as the previous cases and the measurements are first done without lossy objects and then with the head phantom inside the chamber. The total number of platform positions used in this case is 200. Thus, for each platform position three samples are collected, i.e., one for each wall antenna and the total number of measured samples are 600. The results are shown in Figures 5.11 and 5.12 for the empty and the head phantom cases, respectively. The new theory can be applied also in this case by just removing the contribution due to the plates from (4.19). The results show a good agreement between theory and measurements in all frequency ranges and cases. This means that the new formula gives a more accurate estimate of the number of independent samples in the platform stirring case. Figures show that less independent samples are attained compared to the previous cases, but it is reasonable since the total number of measured samples is half compared to the ones considered in the former measurements.

5.5 Best Case Attained

Three sets of measurements have been performed in the whole frequency range in which the reverberation chamber is able to work. The goal is to determine the importance of the different stirring methods in the measurements accuracy. In order to compare all the results, the number of independent samples are plotted by histograms for each measurement case, as shown in Figures 5.13 and 5.14. Each histogram represents the number of independent samples measured for a certain frequency stirring bandwidth. Each sub-band is numbered and divided in bandwidths of 1 GHz (except for the first one that is large 500 MHz). Thus the total frequency range goes from 0.5 to 6 GHz. As can be noticed, the number of independent samples increases with the frequency stirring. However, a high frequency stirring bandwidth hardly ever is used in practical measurements, since the frequency resolution of the measurements decreases. In all the plots can be

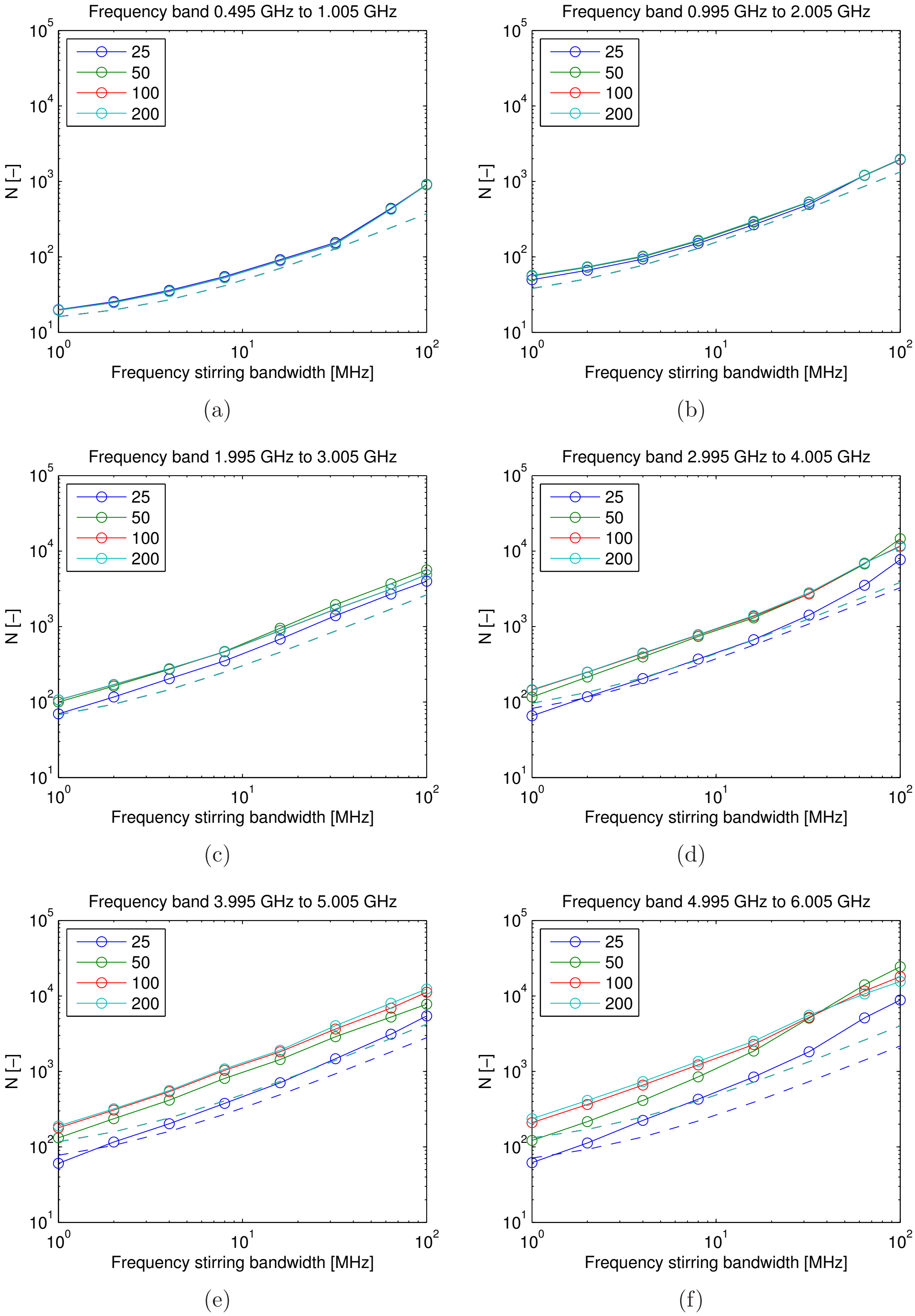

Figure 5.11: Number of independent samples obtained from measurements (continuous lines) and theory (dashed lines) when plate stirring is stopped. The data are processed in logarithmic scale for each sub-band considering 25, 50, 100 and 200 platform positions and using a frequency stirring bandwidth going from 1 MHz to 100 MHz. Empty chamber case.

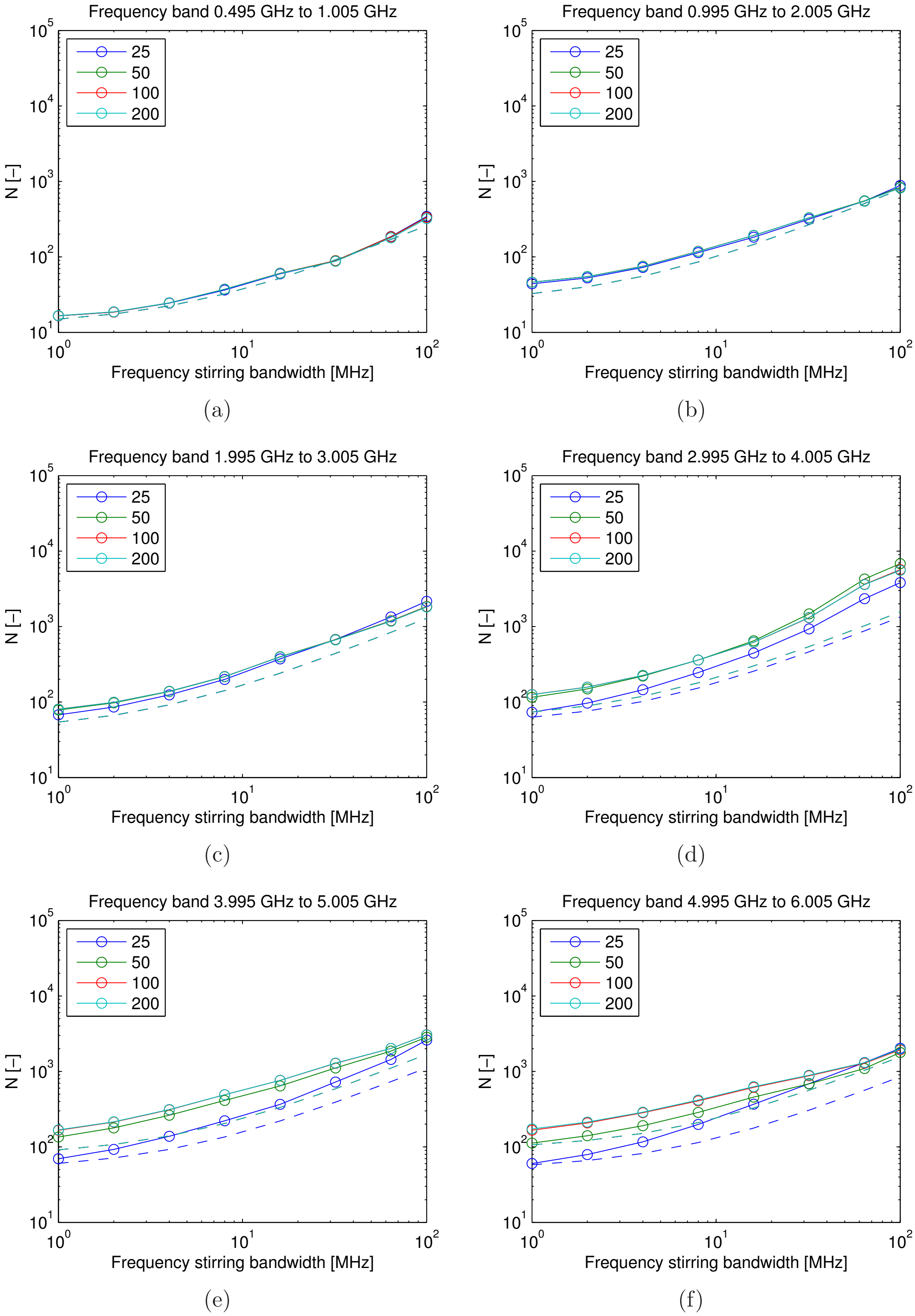

(a) (b) (c) (d) (e) (f)

Figure 5.12: Number of independent samples obtained from measurements (continuous lines) and theory (dashed lines) when plate stirring is stopped. The data are processed in logarithmic scale for each sub-band considering 25, 50, 100 and 200 platform positions and using a frequency stirring bandwidth going from 1 MHz to 100 MHz. Head phantom case.

seen that the first sub-band is the critical one, since the number of independent samples attained is the lowest and in some cases it does not reach 10^2 independent samples if the frequency stirring is not used. Nevertheless, it has to be considered that we are in the limit region in which the chamber works. Few modes are excited and the chamber size is smaller compared to the wavelength such that the direct coupling contribution is greater compared to the other sub-bands. Although the measurements are also done for the empty chamber case, the head phantom case is the one that requires more attention, since the mobile terminals are used to be measured close to lossy objects to ensure that the measurement is done as in real conditions. It is interesting to notice that in the phantom case less independent samples are obtained compared to the empty chamber case. When lossy objects are present inside the RC, the chamber mode bandwidth increases. More modes are excited but it will make more difficult to achieve a decorrelation of those modes. For this reason it is necessary to change the boundary conditions using stirring methods. By comparing the results in Figures for the plates stirring cases, we can see an increase of the number of independent samples when the complex S_{21} stirring is used (Figures (c)). However, the best case can be found when the platform is also used, as shown in Figures 5.13(a) and 5.14(a). It is shown that by introducing the platform stirring a better accuracy can be attained, obtaining a higher number of independent samples.

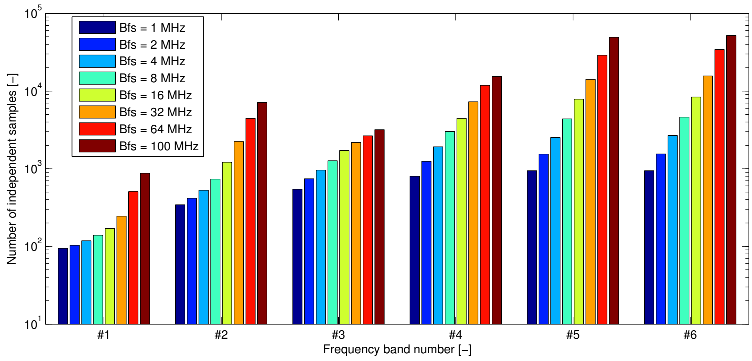

(a) platform and plates case

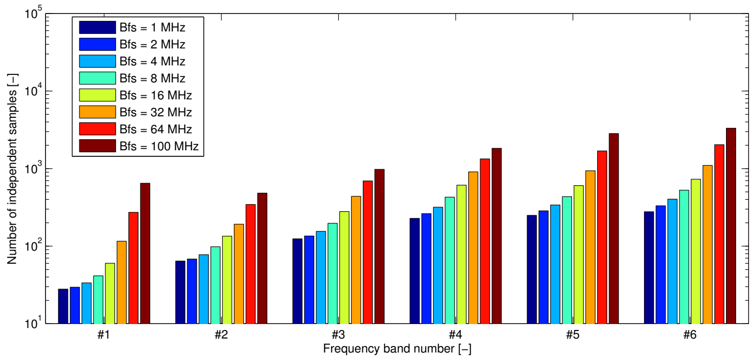

(b) plates case

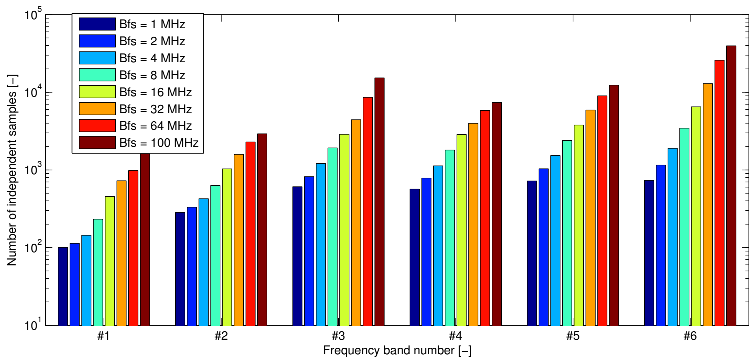

(c) plates case without direct coupling

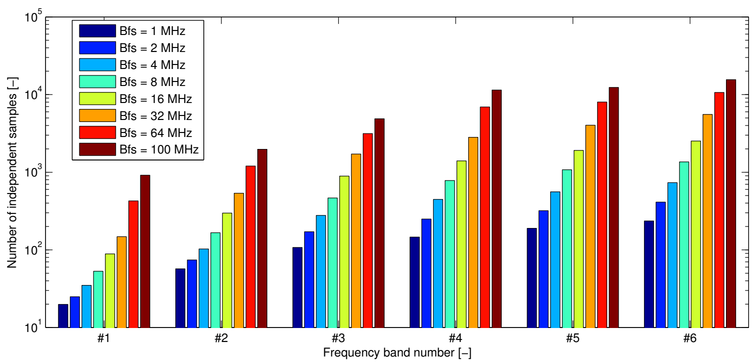

(d) platform case

Figure 5.13: Measured number of independent samples in logarithmic scale represented by histograms for each frequency stirring bandwidth and for each measured sub-band in the empty chamber case.

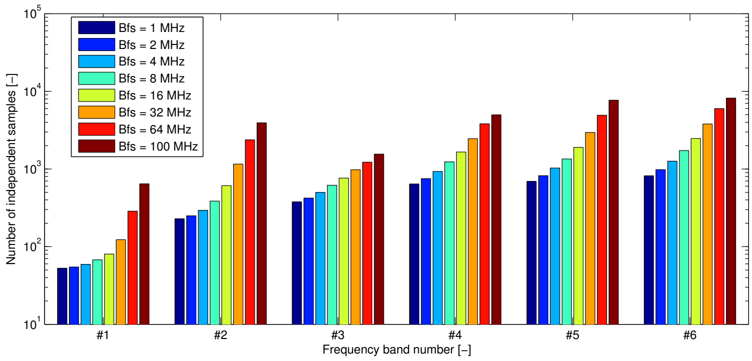

(a) platform and plates case

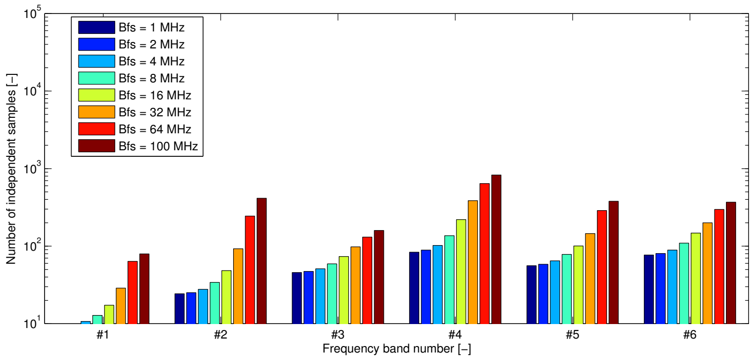

(b) plates case

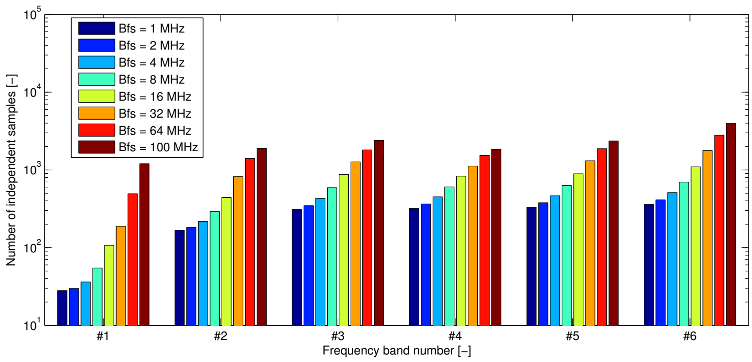

(c) plates case without direct coupling

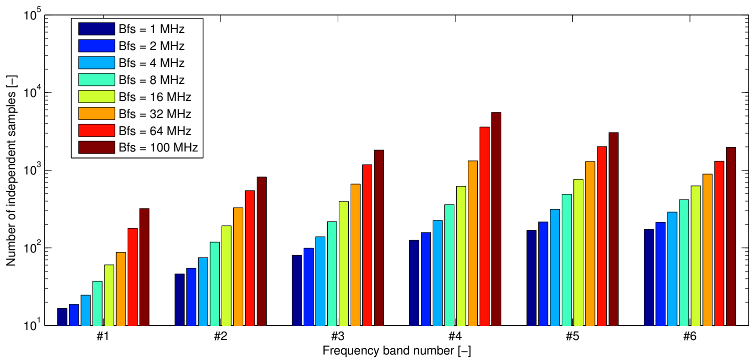

(d) platform case

Figure 5.14: Measured number of independent samples in logarithmic scale represented by histograms for each frequency stirring bandwidth and for each measured sub-band in the head phantom case.

Chapter 6

Conclusions and Future Work

6.1 Conclusions

This thesis work is based on the study of the calibration of the reverberation chamber in order to improve the measurements accuracy for wireless applications. The importance of different stirring techniques in the calibration procedure and a study of the measurements accuracy have been determined for the Bluetest High Performance Reverberation Chamber at Chalmers University of Technology.

This thesis proposed a new physical formula for the estimation of the total number of independent samples when different stirring techniques are used. The new formula considers all the physical and electromagnetic processes involved in the RC and it is also suitable for other reverberation chambers with similar stirring techniques. Experimental validation was provided showing that the new formula works well specifically for the platform stirring case. The results showed good agreement between the number of independent samples obtained from the measured data and the one estimated by the new theoretical formula. For the case in which all the stirring methods were enabled, it was interesting to notice that at the lower frequencies the number of independent samples obtained from the measurements seemed not to match well with the theoretical formula whereas they did at high frequencies, especially for the case in which the measurements were done with the chamber loaded with extra losses. Our investigations in this

direction have been carried out, showing that the reason of this poor matching is due to a residual direct coupling between the receiving and the transmitting antennas. This residual term is shown to be proportional to the wavelength, so that it is negligible only at high frequencies. By removing the residual direct coupling, the agreement at low frequencies was much better for both empty and loaded chamber cases. No changes are noticed at high frequencies where the direct coupling is negligible compared to the power transfer function of the stirred component.
Since the amount of independent samples depends on how well the modes are stirred inside the cavity, a study of the stirring methods effectiveness was also presented in this report. Thereby, by modifying the control software of the chamber, a set of measurements with first platform stirring and then plates stirring stopped were done. The measured data were processed with and without frequency stirring applied. The results confirmed that the number of independent samples increases with the frequency stirring. All the measurements were also performed for both empty chamber and chamber loaded with a head phantom and a comparison of the two cases was proposed. The comparison showed that a lower number of independent samples is obtained in the head phantom case. This is due to the chamber mode bandwidth, since when it increases more modes are excited but it becomes more difficult to independently excite them as well. The results also showed that when the platform is stopped, the number of independent samples decreases. It is reasonable since in this case the AUT, on the platform, is not moving and the direct signals between the AUT and the three transmitting antennas can not be removed. Although those results confirmed that the platform stirring among all stirring methods provides a better accuracy, a solution was proposed in this thesis in order to remove the direct coupling when only the plates are working. The idea was to remove the mean over all the stirrer positions from the complex S_{21}, by 'complex S_{21} stirring'. Results showed an increase of the number of independent samples and a better agreement between theory and measured data in all the frequency ranges.

6.2 Future Work

From the achievements attained in this project some research points can be developed. In this thesis, the measurements are performed in several frequency bands covering the whole working range of the chamber. Thereby, we are able to see the differences in the accuracy from band to band, but not within each band. The next step would be to measure many more times with different positions and orientation of the AUT, evaluating the number of independent samples as function of the frequency. In this direction, it would be interesting to investigate the accuracy at the lower frequencies, in which the number of independent samples is low and the accuracy seems to be affected by the poor mode density even when the frequency stirring is used.

During this work, all the measurements were also done loading the chamber with a head phantom showing that the amount of independent samples is affected by the loading. Thus, more investigations can be carried on to see how the extra losses can influence the accuracy. Measurements with more lossy objects inside the chamber should be performed for this purpose.

The new theoretical formula is a good starting point for the estimation of the number of independent samples. It seems to work well for the platform stirring, but it can be improved for the estimation of the number of independent samples due to the plates and the frequency stirring.

All this work is based on the study of the reverberation chamber in the frequency domain. However, in the wireless communications an important parameter playing a leading role in the system performance is the delay spread, computed in the time domain. Thus, modeling the RC by the temporal approach would be useful to characterize and to test even better wireless channels.

References

[1] P. S. Kildal and K. Rosengren, "Correlation and capacity of MIMO systems and mutual coupling, radiation efficiency, and diversity gain of their antennas: simulations and measurements in a reverberation chamber," *IEEE Communications Magazine*, pp. 104–112, 2004.

[2] K. Rosengren and P. S. Kildal, "Radiation efficiency, correlation, diversity gain and capacity of a six-monopole antenna array for a MIMO system: theory, simulation and measurement in reverberation chamber," *IEE Proc.-Microw. Antennas Propag.*, vol. 152, no. 1, pp. 7–16, 2005.

[3] J. G. Proakis, *Digital Communications*. McGraw Hill.

[4] C. L. Holloway, D. A. Hill, J. M. Ladbury, P. F. Wilson, G. Koepke, and J. Coder, "On the use of reverberation chambers to simulate a rician radio environment for the testing of wireless devices," *IEEE Transactions on Antennas and Propagation*, vol. 54, no. 11, pp. 3167–3177, 2006.

[5] K. Rosengren, P. S. Kildal, C. Carlsson, and J. Carlsson, "Characterization of antennas for mobile and wireless terminals in reverberation chambers: improved accuracy by platform stirring," *Microwave and Optical Technology Letters*, vol. 30, no. 6, 2001.

[6] P. S. Kildal and C. Carlsson, "Detection of a polarization imbalance in reverberation chambers and how to remove it by polarization stirring when measuring antenna efficiencies," *Microwave and Optical Technology Letters*, vol. 34, no. 2, 2002.

[7] D. A. Hill, "Electronic mode stirring for reverberation chambers," *IEEE Transactions on Electromagnetic Compatibility*, vol. 36, no. 4, 1994.

[8] J. Clegg, A. C. Marvin, J. F. Dawson, and S. J. Porter, "Optimization of stirrer designs in a reverberation chamber," *IEEE Transactions on Electromagnetic Compatibility*, vol. 47, no. 4, pp. 824–832, 2005.

[9] N. Wellander, O. Lundén, and M. Bäckström, "Experimental investigation and mathematical modeling of design parameters for efficient stirrers in mode-stirred reverberation chambers," *IEEE Transactions on Electromagnetic Compatibility*, vol. 49, no. 1, pp. 94–103, 2007.

[10] K. Madsén, P. Hallbjörner, and C. Orlenius, "Models for the number of independent samples in reverberation chamber measurements with mechanical, frequency and combined stirring," *IEEE Antennas and Wireless Propagation Letters*, vol. 3, pp. 48–51, 2004.

[11] C. Lemoine, P. Besnier, and M. Drissi, "Advanced method for estimating number of independent samples available with stirrer in reverberation chamber," *Electronics Letters*, vol. 43, no. 16, 2007.

[12] K. Rosengren and P. S. Kildal, "Study of distributions of modes and plane waves in reverberation chambers for the characterization of antennas in a multipath environment," *Microwave and Optical Technology Letters*, vol. 30, no. 6, pp. 386–391, 2001.

[13] E. Mazari, "Physical and statistical models for estimating the number of independent samples in the chalmers reverberation chamber," Chalmers University of Technology, Department of Electromagnetics - Antenna Group, Tech. Rep., 2004.

[14] C. A. Balanis, *Advanced Engineering Electromagnetics*. John Wiley & Sons, 1989.

[15] D. I. Wu and D. C. Chang, "The effect of an electrically large stirrer in a mode-stirred chamber," *IEEE Transactions on Electromagnetic Compatibility*, vol. 31, no. 2, 1989.

[16] P. S. Kildal, "Short course: Characterization of MIMO and diversity antenna systems in reverberation chamber," 2008.

[17] D. A. Hill, "Aperture excitation of electrically large, lossy cavities," *IEEE Transactions on Electromagnetic Compatibility*, vol. 36, no. 3, 1994.

[18] P. Corona, G. Ferrara, and M. Migliaccio, "Reverberating chambers as sources of stochastic electromagnetic fields," *IEEE Transactions on Electromagnetic Compatibility*, vol. 38, no. 3, 1996.

[19] K. Harima, "Statistical characteristics of E-field distribution in a reverberation chamber," *IEICE Transaction Community*, vol. E88-B, no. 8, pp. 3127–3132, 2005.

[20] P. S. Kildal, C. Carlsson, and J. Yang, "Measurement of free-space impedances of small antennas in reverberation chambers," *Microwave and Optical Technology Letters*, vol. 32, no. 2, pp. 112–115, 2002.

[21] P. S. Kildal and C. Orlenius, "Multipath techniques for handset/terminal antennas," in *Antenna Engineering Handbook*, Volakis, Ed. McGraw-Hill, 2007.

[22] R. H. Price, H. T. Davis, and E. P. Wenaas, "Determination of the statistical distribution of electromagnetic field amplitudes in complex cavities," *The American Physical Society*, vol. 48, no. 6, pp. 4716–4729, 1993.

[23] J. G. Kostas and B. Boverie, "Statistical model for a mode stirred chamber," *IEEE Transactions on Electromagnetic Compatibility*, vol. 33, no. 4, pp. 366–370, 1991.

[24] B. H. Liu, D. C. Chang, and M. T. Ma, "Eigenmodes and the composite quality factor of a reverberation chamber," *NBS Technical Note 1066, National Institute of Standards and Technology, Boulder, Colorado 80303-3328, USA*, 1983.

[25] D. A. Hill, "Spatial correlation function for fields in a reverberation chamber," *IEEE Transactions on Electromagnetic Compatibility*, vol. 37, no. 1, pp. 138–145, 1995.

[26] D. A. Hill and J. M. Ladbury, "Spatial correlation functions of fields and energy density in a reverberation chamber," *IEEE Transactions on Electromagnetic Compatibility*, vol. 44, no. 1, pp. 95–101, 2002.

[27] C. Xiaoming and P. S. Kildal, "Relation between coherence bandwidth and average mode bandwidth in reverberation chamber for wireless device measurement," 27-30 October 2008.

[28] C. Orlenius, M. Franzén, P. S. Kildal, and U. Carlberg, "Investigation of heavily loaded reverberation chamber for testing of wideband wireless units," pp. 3569– 3572, 9-14 July 2006.

[29] U. Carlberg, P. S. Kildal, and J. Carlsson, "Numerical study of position stirring and frequency stirring in a loaded reverberation chamber," *submitted to IEEE Transactions on Electromagnetic Compatibility*, 2008.

Ringraziamenti

Prima di tutto, vorrei ringraziare il Prof. Stefano Maci per tutto il supporto e l'aiuto durante l'intero programma di studi. È stato grazie alle sue lezioni e al suo entusiasmo nell'insegnare tali argomenti che io ho potuto maturare la mia passione per l'elettromagnetismo. Per la fiducia che ha posto in me, le devo la mia più sincera gratitudine. Quale studente, è stata una fortuna e un onore poter essere stata seguita da una Persona come lei.

In questi anni di università tante persone hanno contribuito a rendere unico e indimenticabile questo periodo. Non posso che ringraziare con il mio più sentito affetto le mie amiche Daniela e Valentina. Grazie per avermi sempre sostenuto e ascoltata, per aver condiviso con me le gioie di ogni esame superato, ma anche per essermi state vicine nei momenti difficili. Un ringraziamento speciale va anche alle mie care compagne di casa Sara e Giulia. Le nostre chiacchierate, i pranzi, le serate e i momenti di vita quotidiana passati insieme, hanno allietato le mie noiose giornate...e nottate passate sui libri.
Ripensando alle serate trascorse nella magica atmosfera di Piazza del Campo, agli aperitivi, alle cene a base di struncatura, nduja e Amaro del Capo, e a tutte le risate fatte insieme, non posso che ringraziare i miei amici: Raffaele, Morgane, Gumpà, Lucia, Marco, Alessandro, Alberto, Maria 'la greca', Maria 'pdp' e Maria 'di vale'. Grazie a tutti voi per aver contribuito a rendere cosi felici questi anni trascorsi a Siena.

Desidero ringraziare inoltre i miei colleghi, nonchè amici, di università: Marzia, per essere stata la migliore compagna di corso con cui affrontare questi ultimi due anni; Teresa, per aver condiviso con me la straordinaria esperienza in Erasmus; Davide, per la grande amicizia che ci lega fin dal primo anno. Infine, voglio ringraziare anche tutti gli amici e colleghi che hanno iniziato e concluso con me questo lungo percorso.

Un ringraziamento speciale va alle mie grandi amiche: Rosaria, Flavia e Carla. L'affetto che ci lega da ormai tanti anni ha superato le barriere della distanza, tenendoci sempre legate. Sebbene le nostre vite abbiano preso dei percorsi differenti, ho sempre potuto contare su di voi. Grazie per essermi state sempre vicine, pronte a sostenermi in ogni momento della mia vita.
Voglio anche ringraziare tutti i miei amici di Palmi, in particolare Salva, Mico, Graziella e Letterio, per la grande amicizia che ci accompagna fin dai tempi del Liceo. Sono sicura essa resterà indelebile negli anni.

La vita spesso è come un mare travolgente. Grazie, Francesco, per avermi aiutato a nuotare e per essere stato la mia isola quando ho sentito il bisogno di riposare. Grazie per il tuo amore, per la tua pazienza, per avermi aiutato ad affrontare le mie paure e a vedere tutto positivo intorno a me, per essere il mio punto di riferimento, per avermi fatto sognare anche quando ho tenuto gli occhi aperti, e per avermi sempre spronato a superare ciò che a me sembrava insormontabile. Le circostanze forse ci potranno tenere separati, ma i nostri cuori saranno sempre vicini. A te e ai nostri otto anni insieme dedico i miei successi.

Infine, grazie con tutto il cuore a tutta la mia famiglia: i miei genitori, mio fratello, mia nonna, i miei zii e tutti i miei cugini, per avermi fatto crescere in un ambiente pieno di amore e affetto, per essere sempre presenti nella mia vita e per le risate e i momenti di gioia che mi avete regalato in tutti questi anni.
Un ringraziamento speciale va a mia madre e mio padre, per avermi dato la possibilità di arrivare fin qui, per avermi sempre appoggiato e consigliata, lasciandomi decidere e sbagliare da sola e per avermi insegnato i principi e i valori che mi hanno reso la persona attuale. Grazie per la stabilità, la serenità e la sicurezza con cui mi avete fatto crescere. Questa tesi è dedicata a voi.